



# Dynamics of Gene Expression in Single Root Cells of *Arabidopsis thaliana*

Ken Jean-Baptiste,<sup>a</sup> José L. McFaline-Figueroa,<sup>a</sup> Cristina M. Alexandre,<sup>a</sup> Michael W. Dorrity,<sup>a</sup> Lauren Saunders,<sup>a</sup> Kerry L. Bubb,<sup>a</sup> Cole Trapnell,<sup>a</sup> Stanley Fields,<sup>a,b</sup> Christine Queitsch,<sup>a</sup> and Josh T. Cuperus<sup>a,1</sup>

<sup>a</sup>Department of Genome Sciences, University of Washington, Seattle, Washington 98195

<sup>b</sup>Department of Medicine, University of Washington, Seattle, Washington 98195

ORCID IDs: 0000-0001-5768-5993 (K.J.-B.); 0000-0003-4387-1511 (J.L.M.-F.); 0000-0003-0047-0312 (C.M.A.); 0000-0002-7691-6504 (M.W.D.); 0000-0003-4377-4252 (L.S.); 0000-0002-1117-2591 (K.L.B.); 0000-0002-8105-4347 (C.T.); 0000-0001-5504-5925 (S.F.); 0000-0002-0905-4705 (C.Q.); 0000-0002-8019-7733 (J.T.C.)

**Single cell RNA sequencing can yield high-resolution cell-type-specific expression signatures that reveal new cell types and the developmental trajectories of cell lineages. Here, we apply this approach to *Arabidopsis thaliana* root cells to capture gene expression in 3,121 root cells. We analyze these data with Monocle 3, which orders single cell transcriptomes in an unsupervised manner and uses machine learning to reconstruct single cell developmental trajectories along pseudotime. We identify hundreds of genes with cell-type-specific expression, with pseudotime analysis of several cell lineages revealing both known and novel genes that are expressed along a developmental trajectory. We identify transcription factor motifs that are enriched in early and late cells, together with the corresponding candidate transcription factors that likely drive the observed expression patterns. We assess and interpret changes in total RNA expression along developmental trajectories and show that trajectory branch points mark developmental decisions. Finally, by applying heat stress to whole seedlings, we address the longstanding question of possible heterogeneity among cell types in the response to an abiotic stress. Although the response of canonical heat-shock genes dominates expression across cell types, subtle but significant differences in other genes can be detected among cell types. Taken together, our results demonstrate that single cell transcriptomics holds promise for studying plant development and plant physiology with unprecedented resolution.**

## INTRODUCTION

Many features of plant organs such as roots are traceable to specialized cell lineages and their progenitors (Irish, 1991; Petricka et al., 2012). The developmental trajectories of these lineages have been based on tissue-specific and cell-type-specific expression data derived from tissue dissection and reporter gene-enabled cell sorting (Bimbaum et al., 2003; Brady et al., 2007; Li et al., 2016). However, tissue dissection is labor-intensive and imprecise, and cell sorting requires prior knowledge of cell-type-specific promoters and genetic manipulation to generate reporter lines. Few such lines are available for plants other than the reference plant *Arabidopsis thaliana*; (Rogers and Benfey, 2015). Advances in single cell transcriptomics can replace these labor-intensive approaches. Single cell RNA sequencing (RNA-Seq) has been applied to heterogeneous samples of human, worm, and virus origin, among others, yielding an unprecedented depth of cell-type-specific information (Trapnell et al., 2014; Trapnell, 2015; Cao et al., 2017; Packer and Trapnell, 2018; Russell et al., 2018).

Although several examples of single cell RNA-Seq have been performed in *Arabidopsis* (Brennecke et al., 2013; Efroni et al., 2015, 2016), they were restricted to only a few cells or cell types. Few whole organ, single cell RNA-Seq has been attempted in any plant species

(Denyer et al., 2019; Ryu et al., 2019). The *Arabidopsis* examples focused on root tips, finely dissecting the dynamics of regeneration or assaying technical noise across single cells in a single cell type. Thus, a need exists for larger-scale technology that allows a more complete characterization of the dynamics of development across many cell types in an unbiased way. Such technology would increase our ability to assay cell types without reporter-gene-enabled cell sorting, identify developmental trajectories, and provide a comparison of how different cell types respond to stresses or drugs. Several high-throughput methods have been described for sequencing of RNA at a high throughput of single cells. Most of these, including most droplet-based methods, rely on the 3' end capture of RNAs. However, unlike with bulk RNA-Seq, the data from single cell methods can be sparse, such that genes with low expression can be more difficult to study. Here, we take advantage of expression data from root-specific reporter lines in *Arabidopsis* (Bimbaum et al., 2003; Brady et al., 2007; Cartwright et al., 2009; Li et al., 2016) to explore the potential of single cell RNA-Seq to capture the expression of known cell-type-specific genes and to identify new ones. We focus on roots of mature seedlings and probe the developmental trajectories of several cell lineages.

## RESULTS

### Single-Cell RNA-Seq of Whole *A. thaliana* Roots Reveals Distinct Populations of Cortex, Endodermis, Hair, Nonhair, and Stele Cells

We used whole *Arabidopsis* roots from 7d-old seedlings to generate protoplasts for transcriptome analysis using the 10×

<sup>1</sup> Address correspondence to: cuperusj@uw.edu or queitsch@uw.edu. The author responsible for distribution of materials integral to the findings presented in this article in accordance with the policy described in the Instructions for Authors (www.plantcell.org) is: Josh T. Cuperus (cuperusj@uw.edu).  
www.plantcell.org/cgi/doi/10.1105/tpc.18.00785

## IN A NUTSHELL

**Background:** Plants are made up of many different types of cells with different roles. These cells can be identified based on the types of genes they express, which are important to their roles. Many approaches have been used to study specific types of cells in Arabidopsis roots, including methods to express fluorescence proteins in only some types of cells. Newer technologies can capture thousands of individual cells at the same time, measuring the total RNA molecules in each cell. We have applied this single-cell RNA-seq technology to the Arabidopsis root.

**Question:** We sought to answer several important questions, but also bring new technological advances to plant systems. We asked the biological questions: Can distinct cell-types be resolved using single-cell RNA-seq of a whole Arabidopsis root? Can developmental information be understood using single-cell RNA-seq?

**Findings:** We identified all the major cell types in Arabidopsis roots based on each cell type's unique RNA expression profile. We also visualized the developmental trajectory of many cell types, finding differences between young and old cells within the same tissue, and identifying transcription factors that were expressed specifically in young or old cells. We captured distinct, small populations of cells, including ones actively dividing. Lastly, we applied an abiotic stress, heat shock, to these roots. We found drastic changes in expression, some of which were cell-type specific. Cells in the exterior layers of the root had larger changes in expression than did interior cell types.

**Next steps:** Our work shows that it is possible to discern different cells with single cell RNA-seq in Arabidopsis roots, so in the future we hope to apply the same technique to Arabidopsis shoots, and other plants such as camelina, sorghum, and maize.

Genomics platform (Supplemental Figure 1A). We captured 3,121 root cells to obtain a median of 6,152 unique molecular identifiers (UMIs) per cell. UMIs here are 10 base random tags added to the cDNA molecules that allow us to differentiate unique cDNAs from PCR duplicates. These UMIs corresponded to the expression of a median of 2,445 genes per cell and a total of 22,419 genes, close to the gene content of *A. thaliana*. Quality measures for sequencing and read mapping were high. Of the ~79,483,000 reads, 73.5% mapped to The Arabidopsis Information Resource (TAIR10) Arabidopsis genome assembly, with 67% of these annotated transcripts. These values are well within the range reported for droplet-based single cell RNA-Seq in animals and humans.

For data analysis, we applied Monocle 3, which orders transcriptome profiles of single cells in an unsupervised manner without a priori knowledge of marker genes (Trapnell et al., 2014; Qiu et al., 2017a, 2017b). We used the 1,500 genes in the data set (Supplemental Data Set 1) that showed the highest variation in expression (Supplemental Figure 1B). For unsupervised clustering, we used 25 principal components (PCs). These 25 PCs accounted for 72.5% of the variance explained by the first 100 PCs, with the first PC explaining 11% and the 25th PC explaining 0.9% (Supplemental Figure 1C). Cells were projected onto two dimensions using the Uniform Manifold Approximation and Projection (UMAP) method (McInnes et al., 2018) and clustered, resulting in 11 clusters (Figure 1A; Blondel et al., 2008). Most clusters showed similar levels of total nuclear mRNA, although clusters 9 and 11 were exceptions with higher levels (Supplemental Figure 1D). Because some of the UMAP clusters, specifically clusters 9 and 11, consisted of cells that had higher than average amounts of nuclear mRNA, we were concerned that these clusters consisted merely of cells that were doublets, i.e. two (or more) cells that received the same barcode and that resulted in a hybrid transcriptome. As cells were physically separated by digestion, it was possible that two cells remained partially attached. To identify potential doublets in our data, we performed a doublet analysis using Scrublet (Wolock et al., 2018), which uses

barcode and UMI information to calculate the probability that a cell is a doublet. This analysis identified only six cells, of 3,021 cells analyzed, as doublets, spread across multiple UMAP clusters and multiple cell types (Supplemental Figure 1E). Overall, given the low number of doublets, we did not attempt to remove these cells.

To assign these clusters to cell types, we performed three complementary analyses relying on two expression data sets from tissue-specific and cell-type-specific reporter lines: an earlier one generated with microarrays (Brady et al., 2007; Cartwright et al., 2009) and a more recent one generated with RNA-Seq and a greater number of lines (Li et al., 2016). First, we compared the microarray expression data for each reporter line to the gene expression values in each single cell, using Spearman's rank correlations to assign each cell a cell-type identity based on highest correlation of gene expression (Figure 1B; Supplemental Data Set 2; Brady et al., 2007; Cartwright et al., 2009). Second, we compared the RNA-Seq expression data to the gene expression values in each single cell by Pearson's correlation (Li et al., 2016; Supplemental Figure 2A). Third, we examined the expression of 530 cell-type-specific marker genes (Brady et al., 2007) by defining seven marker gene clusters with *k*-means clustering and calculating their average expression for each cell. We then compared each cell's UMAP Louvain component cluster assignment (Figure 1A) with its marker-gene-based assignment. Louvain components were derived using the Louvain method for community detection (Blondel et al., 2008), which is implemented in Monocle 3. Unlike *k*-means clustering for which the user provides the desired number of clusters to partition a data set, Louvain clustering optimizes modularity (i.e. the separation of clusters based on similarity within a cluster and among clusters), aiming for high density of cells within a cluster compared with sparse density for cells belonging to different clusters. The 11 clusters presented in Figure 1A optimized the modularity of the generated expression data and were not defined by us.

In general, the UMAP clusters showed high and cluster-specific expression of marker genes. For example, cells in cluster 10

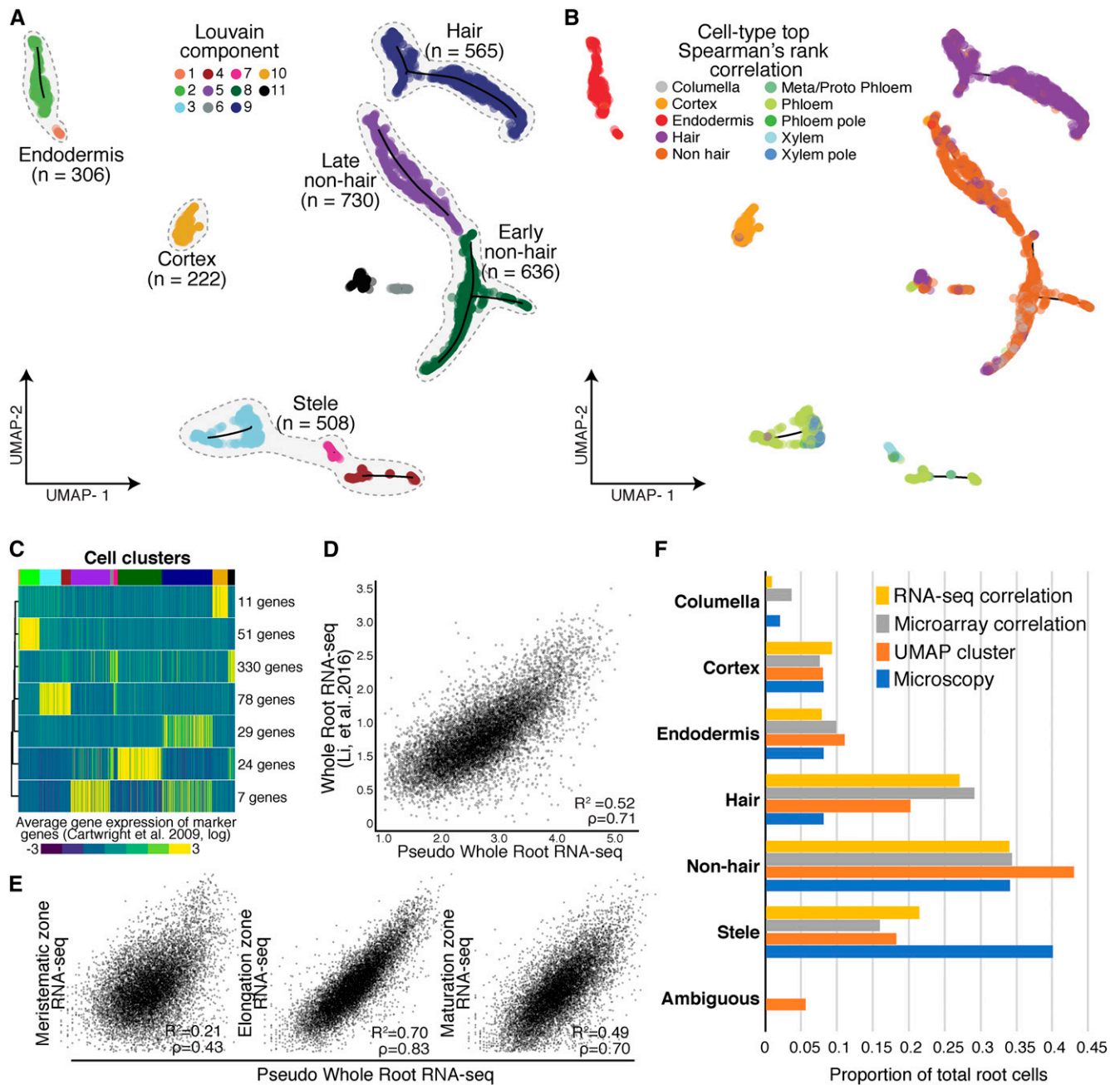


**Figure 1.** Annotation of Cell and Tissue Types for Single Cell RNA-Seq of Whole Arabidopsis Roots.

(A) Root cells were clustered and projected onto two-dimensional space with UMAP (McInnes and Healy, 2018). Solid circles represent individual cells; colors represent their respective Louvain component. Monocle 3 trajectories (black lines) are shown for clusters in which a trajectory could be identified.

(B) Solid circles represent individual cells; colors indicate cell and tissue type based on highest Spearman's rank correlation with sorted tissue-specific bulk expression data (Brady et al., 2007; Cartwright et al., 2009).

(C) Known marker genes (Brady et al., 2007; Cartwright et al., 2009) were used to cluster single cell gene expression profiles based on similarity. The expression of 530 known marker genes was grouped into seven clusters, using  $k$ -means clustering. Mean expression for each cluster (rows) is presented for each cell (columns). Cells were ordered by their respective Louvain component indicated above by color (see (A), starting at component 1 at left). Number of genes in each cluster is denoted at right.

(D) Single cell RNA-Seq pseudo-bulked expression data are compared with bulk expression data of whole roots (Li et al., 2016).

(E) Single cell pseudo-bulk expression data are compared with bulk-expression data of the three developmental regions of the Arabidopsis root (Li et al., 2016).

(F) Proportions of cells as annotated by either UMAP (A), Spearman's rank correlation (B), or Pearson's rank (in Supplemental Figure 2), are compared with proportions determined by microscopy (Brady et al., 2007; Cartwright et al., 2009).

showed high and specific mean expression of cortex marker genes (Figure 1C; Supplemental Figure 3; Supplemental Data Set 3). Both expression correlations and marker gene expression allowed us to assign the Louvain components to five major groups: root hair cells, nonhair cells (containing both an early and late cluster), cortex cells, endodermis cells, and stele cells (containing both xylem and phloem cells; Figure 1A). Although some cells were most highly correlated in expression with the cell-type columella in Spearman's rank tests and RNA-Seq Pearson's correlation, these cells coclustered with nonhair cells (Figure 1B; Supplemental Figure 2). This finding is consistent with bulk RNA-Seq data of sorted cells (Li et al., 2016). Specifically, the *PET111* (columella)-sorted bulk RNA-Seq data are most similar to bulk RNA-Seq data sorted for *GLABRA2* (*GL2*) and *WEREWOLF* (*WER*; Li et al., 2016), both of which mark nonhair cells (Petricka et al., 2012). Therefore, these cells were grouped as early nonhair cells with other nonhair cells in Louvain component 8. As their expression values were best correlated with RNA-Seq data for *WER*-sorted cells, they likely represent a mix of early nonhair and lateral root cap cells, which have very similar expression profiles (Supplemental Figure 2).

We assessed the extent to which combined single cell root expression data resembled bulk whole-root expression data (Figures 1D and 1E; Li et al., 2016). We observed strong correlations between these two data sets (Pearson's correlation coefficient  $R^2 = 0.52$ , Spearman's  $\rho = 0.71$ ). We also compared the combined single cell expression data to three bulk expression data sets representing the major developmental zones in the Arabidopsis root: the meristematic zone, the elongation zone, and the maturation zone (Figure 1E). We observed the highest correlation of single cell and bulk expression in the elongation zone ( $R^2 = 0.70$ ,  $\rho = 0.83$ ) and a lower correlation in the maturation zone ( $R^2 = 0.58$ ,  $\rho = 0.70$ ). This observation is surprising given the more mature developmental stage of the harvested roots (Supplemental Figure 1A), and likely reflects that younger cells are more easily digested during protoplasting and contribute in greater numbers to the gene expression data. As expected, single cell and bulk expression were poorly correlated in the meristematic zone ( $R^2 = 0.11$ ,  $\rho = 0.43$ ), as meristematic tissue accounts for only a small proportion of mature roots. Furthermore, we compared tissue-specific expression (Li et al., 2016) to expression both in the annotated cell clusters and in cells expressing appropriate marker genes. In general, we found strong correlations among these data sets, suggesting that the clusters are annotated correctly (Supplemental Table 1).

We also compared the relative representation of root cell types between our data set and estimates based on microscopy studies (Figure 1F; Brady et al., 2007; Cartwright et al., 2009). Independent of annotation method, we observed the expected numbers of cortex (222 Spearman's/233 UMAP), endodermis (306/304), nonhair cells (1,201/1,061), and columella cells (111/no UMAP cluster). Hair cells (565/898) were overrepresented whereas stele cells (508/490) were underrepresented, possibly reflecting a bias in the protoplast preparation of whole root tissue.

Protoplasting, the removal of the plant cell wall, alters the expression of 346 genes (Birbaum et al., 2003); 76 of these genes were included in the 1,500 genes with the highest variation in expression (Supplemental Data Set 1; Supplemental Figure 1B)

that we used for clustering. Some of the 76 genes showed cell-type-specific expression. To exclude the possibility that the expression pattern of these genes produced artifactual clusters and cell-type annotations, we removed them from the analysis and reclustered, which resulted in a similar UMAP visualization, with similar numbers of Louvain components and cell types.

### Single Cell RNA-Seq Identifies Novel Genes with Cell-Type- and Tissue-Type-Specific Expression

Some marker genes are not expressed exclusively in a single cell type, making it desirable to identify additional genes with cell-type-specific expression. First, we confirmed the high and cluster-specific expression of well-known marker genes (Figure 2A; Supplemental Figure 4; Li et al., 2016) such as the root-hair-specific *COBRA-LIKE 9* (*COBL9*), the endodermis-specific *SCARECROW* (*SCR*) and the three stele-specific genes *MYB46* (xylem-specific), *ALTERED PHLOEM DEVELOPMENT* (*APL*; phloem-specific), and *SUCROSE-PROTON SYMPORTER 2* (*SUC2*; phloem-specific). The nonspecific expression of the quiescent center cell marker genes *WUSCHEL RELATED HOMEODOMAIN 5* (*WOX5*) and *AGAMOUS-LIKE 42* (*AGL42*) is likely due to the failure to capture sufficient numbers of these rare cells. The nonspecific expression of *WOODEN LEG* (*WOL*) and the more heterogeneous pattern of both *WER* and *GL2* expression have been previously observed (Brady et al., 2007; Winter et al., 2007).

Second, to find novel marker genes, we identified genes with significantly different expression within and among Louvain component clusters by applying the Moran's I test implemented in Monocle 3. We found 317 genes with cluster-specific expression, 164 of which were novel, including at least one in each cluster (Figure 2A; Supplemental Data Set 4). Using cell-type annotations rather than Louvain clusters, we identified 510 genes with cell-type-specific expression, of which 317 overlapped with the Louvain component cluster-specific expression genes, as well as an additional 125 novel genes, some of which have been implicated in the development of a cell lineage in targeted molecular genetics studies.

For example, the stele-specific gene AT1G68810 (*ABNORMAL SHOOT 5*; stele; Figure 2A) encodes a basic helix-loop-helix (bHLH) protein that promotes vascular cell division and differentiation as part of a heterodimer with a second bHLH protein, *LONESOME HIGHWAY* (Ohashi-Ito et al., 2014; Katayama et al., 2015). Another stele-specific gene, AT4G36160 (*VASCULAR-RELATED NAC-DOMAIN 2*; cluster 7; Figure 2A), encodes a Class IIB Nascent polypeptide-Associated Complex (NAC)-domain transcription factor that contributes to xylem vessel element differentiation by promoting secondary cell wall formation and programmed cell death (Tan et al., 2018). In tissue-specific bulk data (Brady et al., 2007; Winter et al., 2007), both genes show xylem-specific expression consistent with their biological functions; *ABNORMAL SHOOT 5* expression is high only in the meristematic and elongation zones, whereas *VASCULAR-RELATED NAC-DOMAIN 2* expression starts in the elongation zone and persists throughout the maturation zone. Other genes, not previously implicated in root development, show tissue-specific bulk expression patterns consistent with the single cell data. For example, AT1G54940 (*GLUCURONIC ACID SUBSTITUTION OF*

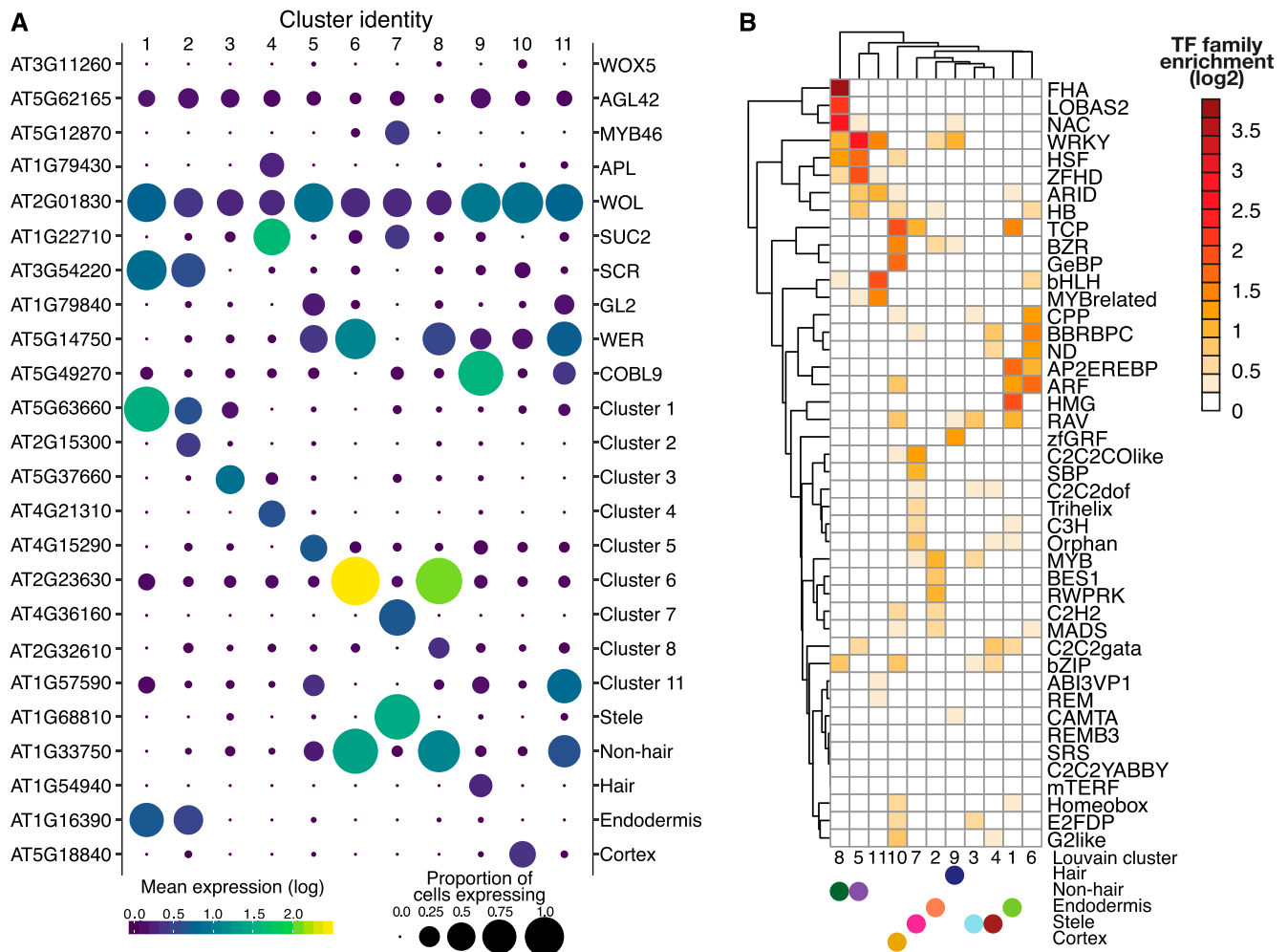


**Figure 2.** Novel Cluster-Specific and Tissue-Specific Genes and Enriched Transcription Factor Motifs.

**(A)** The proportion of cells (circle size) and the mean expression (circle color) of genes with cluster-specific and tissue-specific expression are shown, beginning with known marker genes labeled with their common name (right) and their systematic name (left). For novel genes, the top significant cluster-specific genes are shown, followed by the top significant tissue-specific genes; both were identified by principal graph tests (Moran's I) as implemented in Monocle 3. Note the correspondence between Louvain components and cell and tissue types. For all novel cluster-specific and tissue-specific genes, see Supplemental Table 3.

**(B)** Enrichments of known transcription factor motifs (O'Malley et al., 2016) 500 bp upstream of genes with cluster-specific expression compared with genome background. Motifs are specific to transcription factor gene families rather than individual genes. The plot is clustered based on similarity in enrichments with Louvain components and the cell and tissue types (solid circles) indicated.

*XYLAN4*), which encodes a xylan glucuronosyltransferase (Mortimer et al., 2010; Lee et al., 2012), was specifically expressed in hair cells (cluster 9/hair; Figure 2A) and is most highly expressed in cells destined to become hair cells in the elongation zone and in differentiated hair cells in the maturation zone (Brady et al., 2007; Cartwright et al., 2009).

### Expression of Some Factor Genes Shows High Correlation with Specific Cell Types

We asked whether we could identify transcription factors that may contribute to the cluster-specific expression patterns. To do so, we tested for transcription factor motif enrichments in the proximal

regulatory regions of genes with cluster-specific expression, examining 500 bp upstream of the transcription start site (Sullivan et al., 2014; Alexandre et al., 2018) and a comprehensive collection of Arabidopsis transcription factor motifs (O'Malley et al., 2016). This analysis revealed significant transcription factor motif enrichments among clusters and annotated major tissues and cell types (Figure 2B).

As transcription factors in Arabidopsis often belong to large gene families without factor-specific motif information (Riechmann et al., 2000), it is challenging to deduce the identity of the specific transcription factor that drives cluster-specific transcription factor motif enrichment and expression. As an approximation, we examined transcription factor genes that were expressed in the cluster or



tissue in which a significant enrichment of their motif was found, or in neighboring cell layers (some factors move between cells; Petricka et al., 2012; Supplemental Data Set 4). We focused first on the small *BRI1-EMS Suppressor (BES)/Brassinazole-Resistant (BZR) Homolog (BEH)* gene family whose motif was specifically enriched in cortex cells (cluster 10). Of the six genes (*BEH1/AT3G50750*, *BEH2/AT4G36780*, *BEH3/AT4G18890*, *BEH4/AT1G78700*, *BES1/AT1G19350*, and *BZR1/AT1G75080*), the single recessive *beh4*, *bes1*, and *bzr1* mutants exhibit altered hypocotyl length (Lachowiec et al., 2018). Double mutant analysis suggests partial functional redundancy, which agrees with our observation of overlapping expression patterns for these genes across cell types (Supplemental Figures 5A and 5B). By contrast, neither *beh1* and *beh2* single mutants nor the respective double mutant show phenotypic defects (Lachowiec et al., 2018). However, *BEH2* was the most highly expressed *BZR/BEH* family member across clusters and annotated root tissue and cell types (Supplemental Figures 5A and B). Although *BEH4*, the most ancient family member with the strongest phenotypic impact, showed cortex-specific expression, none of the *BZR/BEH* genes showed significance for cluster-specific expression, suggesting that combinations of family members, possibly as heterodimers, may result in the corresponding motif enrichment in cortex cells (Supplemental Figures 5A and 5B). In particular, *BES1* and *BZR* expression was highly correlated, consistent with these genes being the most recent duplicates in the family (Supplemental Figure 5C; Lachowiec et al., 2013; Lan and Pritchard, 2016).

In contrast with the *BEH/BZR* gene family, we found stronger cluster specificity for some genes containing TCP transcription factor motifs in their promoters. The TCP motif was strongly enriched in cortex (cluster 10), endodermis (cluster 1), and stele (cluster 7). Of the 24 TCP transcription factor genes, we detected expression for eight. Of these, *TCP14* (AT3G47620) and *TCP15* (AT1G69690) were expressed primarily in stele (clusters 7 and 4), although this cluster-specific expression was not statistically significant (Figure 2B; Supplemental Figures 5D and 5E; Supplemental Data Set 4). *TCP14* and *TCP15* encode class-I TCP factors thought to promote development. Acting together, *TCP14* and *TCP15* promote cell division in young internodes (Kieffer et al., 2011), seed germination (Resentini et al., 2015), cytokinin and auxin responses during gynoecium development (Lucero et al., 2015), and repression of endoreduplication (Peng et al., 2015). Both genes are expressed in stele in bulk tissue data (Brady et al., 2007; Winter et al., 2007), with *TCP14* expression also observed in the vasculature by in situ hybridization (Tatematsu et al., 2008). *TCP14* can affect gene expression in a non-cell-autonomous manner.

To further investigate the co-occurrence of cluster-specific transcription factor motif enrichments with transcription factor expression, we next examined the novel genes with significant cluster-specific expression. Eight of these encode transcription factors with corresponding highly enriched cluster-specific binding motifs. For one of these, *BEARSKIN2* (AT4G10350), cluster-specific expression coincided with enrichment of the NAC transcription factor family motif (cluster-8, nonhair, and lateral root cap cells; Figure 2B). *BEARSKIN2* encodes a Class IIB NAC transcription factor implicated in root cap maturation together with *BEARSKIN1* and *SOMBRERO*. Class IIB NAC transcription factors are thought to contribute to terminal cell differentiation accompanied by strong cell wall modifications (Bennett et al., 2010).

In our data, *BEARSKIN2* was most highly expressed in cluster 8 (nonhair and lateral root cap cells) and less so in cluster 6 (Supplemental Data Set 4).

### Clustering Stele Cells Identifies Novel Genes with Cell-Type-Specific Expression in the Vasculature

Our initial attempts to annotate and separate cell types within stele tissue with marker gene expression or Spearman's rank correlations failed. Instead, we separately clustered stele cells to reveal six subclusters upon UMAP visualization, with five subclusters containing more than 40 cells. Their annotation via Spearman's rank correlation with sorted bulk data was not successful; however, using well-established marker genes expression, we detected cluster-specific expression patterns (Figures 3A and 3B).

Cells closely related to the xylem pole pericycle constituted the largest group of cells (205 cells); phloem pole pericycle cells were the second largest (84 cells). The high number of pericycle cells likely reflects our experimental procedure, as these cells reside on the exterior of the vascular bundle. Both phloem and xylem clusters showed similar numbers of cells (77 cells and 72 cells, respectively); the phloem companion cells formed a distinct cluster. We observed the expected subcluster expression for several known genes and marker genes and identified novel genes with subcluster-specific expression (Figures 3C and 3D; Supplemental Data Set 1). Although there was some discrepancy, especially for the *APL* gene, which is expressed in both companion and phloem cells (Figure 3C), this is largely due to missing data.

### Pseudotime Trajectories Coincide with the Development Stages of Cortex, Endodermis, and Hair Cells

We next sought to visualize the continuous program of gene expression changes that occurs as each cell type in the root differentiates. Because whole roots contain a mix of cells at varying developmental stages, we reasoned that our experiment should have captured a representative snapshot of their differentiation. Monocle not only clusters cells by type but also places them in "pseudotime" order along a trajectory that describes their maturity. To make these trajectories, Monocle 3 learns an explicit principal graph from the single cell expression data through reversed graph embedding, an advanced machine learning method (Trapnell et al., 2014; Qiu et al., 2017a, 2017b). To dissect the developmental dynamics of individual clusters, we first focused on the well-defined root-hair cells, in which combined single cell expression values highly correlated with those from bulk protoplasts sorted for expression of the *COBL9* root-hair marker gene (Supplemental Table 1). To annotate the unsupervised trajectory that Monocle 3 created for hair cells, we used the Spearman's rank test to compare expression in all cells to bulk expression data representing 13 different developmental stages in root tissues from all the available sorted cell types (Supplemental Figure 6; Brady et al., 2007; Cartwright et al., 2009). Each cell was assigned the developmental stage and cell type most correlated with its expression values (Figure 4A). The hair cells with the earliest developmental stage assignment were designated as the root of

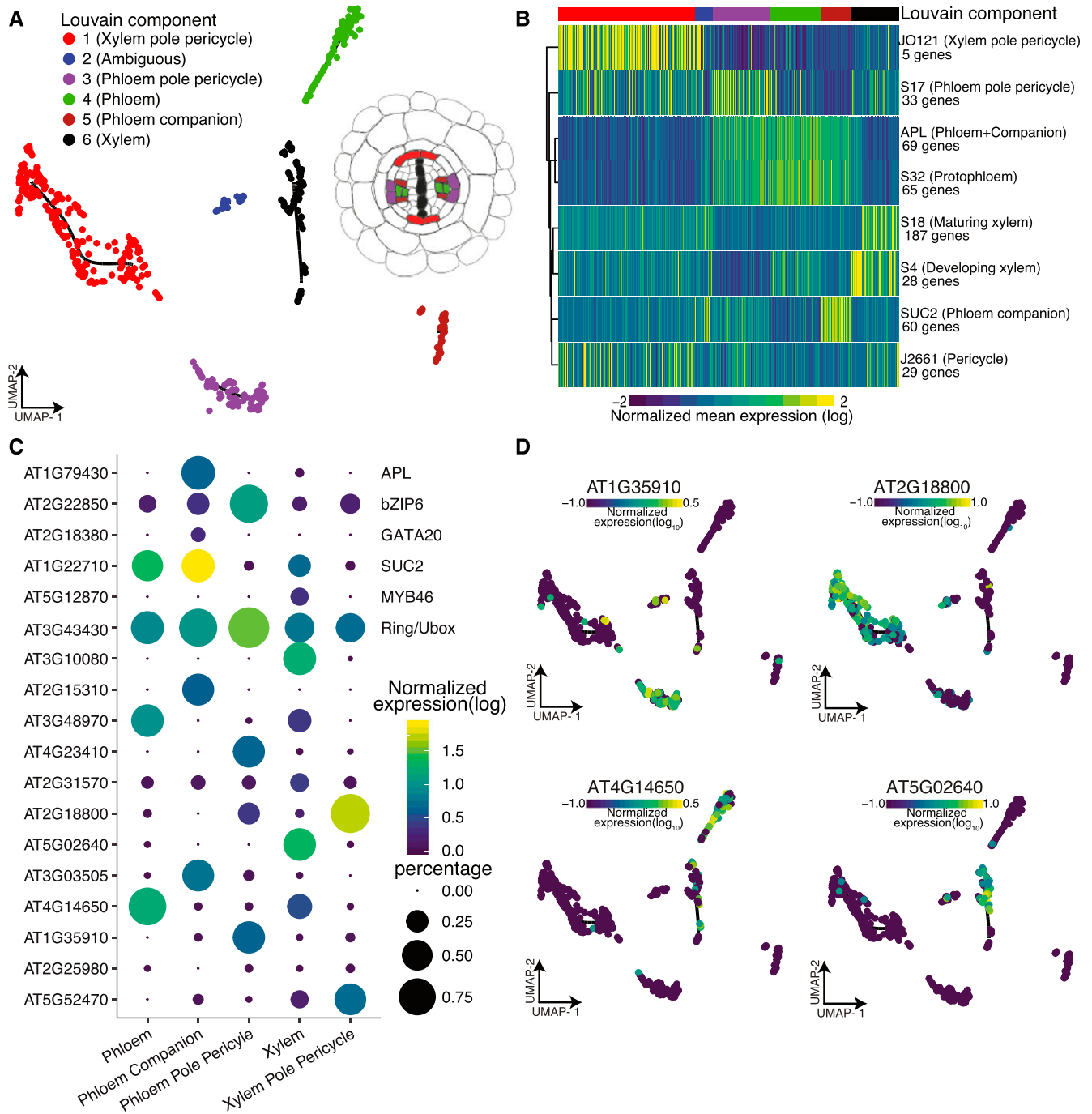


**Figure 3.** Reclustering of Stele Cells Yields Distinct Subclusters of Vasculature Cell Types.

(A) Cells initially annotated as stele tissue were reclustered, resulting in six distinct subclusters cells, five of which contained >40 cells. (B) Mean expression for previously identified cell-type-specific genes (Cartwright et al., 2009) in each cell is shown, allowing annotation of stele subcluster identities as shown in (A). (C) Proportion of cells (circle size) and mean expression (circle color) of genes with cluster-specific and tissue-specific expression are shown, starting with known marker genes at the top, labeled with their common name (right) and their systematic name (left). Below, novel significant tissue-specific genes are shown with their systematic names, identified by principal graph tests (Moran’s I) as implemented in Monocle 3. (D) Example expression overlays for cluster-specific genes identified by the principal graph test in (C).

the trajectory. Next, pseudotime was calculated for all other hair cells based on their distance from the root of the trajectory (Figure 4B). We compared this calculated pseudotime with the most highly correlated developmental assignment from bulk data, finding close agreement (Figure 4B). Examples of genes that are expressed early or late in pseudotime in the UMAP hair cluster are shown in Figure 4C.

Hair cells undergo endoreduplication as they mature, resulting in up to 16N genomic copies in the developmental stages assayed (Bhosale et al., 2018). Although endoreduplication is thought to increase transcription rates (Bourdon et al., 2012), general transcription might decrease as hair-cell-specific genes become more highly expressed during hair-cell differentiation. Single cell RNA-Seq affords us the opportunity to explore whether transcription rates differ across development. Single cell RNA-Seq can measure both relative expression (as in bulk RNA-Seq) and the total number of RNA molecules per cell. The total amount of cellular mRNA was drastically reduced across hair-cell development (Figure 4D). This result may be due to technical bias; for example, gene expression in larger, endoreduplicated cells may be more difficult to assess with this droplet-based method. If so, the observed reduction in captured transcripts should affect all genes more or less equally. Alternatively, this observation may reflect hair-cell differentiation, whereby transcription of hair-cell-specific genes should remain unaffected or increase over pseudotime. Our results support the latter scenario as transcription of hair-cell-specific genes appears to increase over pseudotime, consistent with these cells undergoing differentiation toward terminally differentiated hair cells (Figure 4E; Supplemental Figure 7A).

To further explore this transcriptional dynamic, we calculated RNA velocity (La Manno et al., 2018), a measure of the transcriptional rate of each gene in each cell of the hair-cell cluster. RNA velocity takes advantage of errors in priming during 3' end reverse transcription to determine the splicing rate per gene and cell. It compares nascent (unspliced) mRNA to mature (spliced) mRNA; an overall relative higher ratio of unspliced to spliced transcripts indicates that transcription is increasing. In our data, only ~4% of reads were informative for annotating splicing rates, a lower percentage than what has been used in mammalian cells for velocity analyses, and thus our results may be less reliable. Based on data for 996 genes, mean RNA velocity increased across pseudotime (Supplemental Figure 7B,  $P = 2.2 \times 10^{-16}$  linear model,  $\rho = 0.73$ ). This increase in velocity was associated with the predicted changes in endoreduplication (Bhosale et al., 2018), especially between the 4N and 8N stages (Supplemental Figure 7C; Tukey's multiple comparison  $P$  value = 0.0477).

We also observed developmental signals in other cell types, including cortex and endodermis (Figures 5A to 5D; Supplemental Figure 8). Combined single cell expression values for cortex cells highly correlated with those from bulk protoplasts sorted for expression of the *COR* cortex marker gene (Figure 5B;  $R^2 = 0.74$ ,  $\rho = 0.86$ ). As Monocle 3 did not identify a trajectory for cortex cells in the context of all cells, we isolated the cortex cells and reperformed UMAP dimensionality reduction, clustering, and graph embedding (Supplemental Data Set 1). Each cortex cell was assigned a developmental stage based on its Spearman's rank correlation with bulk expression data (Brady et al., 2007;

Cartwright et al., 2009). Cortex cells with the earliest developmental signal were designated as the root of the cortex trajectory, and pseudotime was assigned to the remaining cortex cells based on their distance from the root (Figures 5A to 5D; Supplemental Figure 6). As pseudotime increased for cortex cells, so did their age, indicating good agreement of the trajectory with developmental bulk RNA-Seq data. Although we observed some decrease in total RNA expression and increased expression in cell-type-specific genes for endodermis, we did not see a clear pattern of change in total RNA across cortex pseudotime (Supplemental Figures 8 and 9).

We asked whether we could assign the transcription factors that drive gene expression along these developmental trajectories in early and late hair, cortex, and endodermis cells. As before, we first analyzed transcription factor motif enrichments and then explored the expression of the corresponding transcription factor gene families. Indeed, for most developmentally enriched transcription factor motifs, we could pinpoint candidate transcription factors that are expressed either early or late. For example, the APE-TALA2/ethylene-responsive element binding protein transcription factor family is one of the largest in Arabidopsis (Riechmann et al., 2000), with nearly 80 covered in our data set; of these, only four (AT2G25820, AT5G65130, AT1G36060, and AT1G44830) showed strong expression in late hair cells (Figures 4F and 4G; Supplemental Figure 10). One of these, AT1G36060 (Translucent Green), regulates expression of aquaporin genes (Zhu et al., 2014). Overexpression of this gene confers greater drought tolerance (Zhu et al., 2014), consistent with its expression in older hair cells. Similar examples of developmental stage-specific motif enrichments with corresponding transcription factor expression were also found for cortex and endodermis (Figures 5E and 5F; Supplemental Figures 8 and 10).

### Branch Points in Developmental Trajectories Mark Developmental Decisions

Although a developmental trajectory that reflects the differentiation from early to late cells within a cell type should be branchless, we did observe some branch points, for example in Louvain component 8, affording us the opportunity to explore their biological relevance. As discussed, Louvain component 8 contains early nonhair cells and likely some lateral root cap cells. To further explore the cells within the branch, we performed a principal graph test, comparing their expression profiles to those of cells elsewhere in the cluster (Figure 6A). We found that cells within the branch were significantly enriched for expression of genes involved in cell plate formation, cytokinesis, and cell cycle. We explored this enrichment for cell-cycle annotations by comparing expression of previously identified core cell-cycle genes (Gutierrez, 2009) in cells within the branch to cells in the rest of the cluster, finding many core cell-cycle genes, in particular many G2 genes, to be specifically expressed in branch cells (Figure 6B). Among these genes were several of the cyclin-dependent kinase (CDK) B family members that direct the G2 to M transition. Two CDK subunits (encoded by *CKS1* and *CKS2*), thought to interact with several CDK family members, were also specifically expressed in branch cells (Vandepoele et al., 2002). Other branch-cell-specific genes included *AURORA1* (*AUR1*) and *AUR2*, both



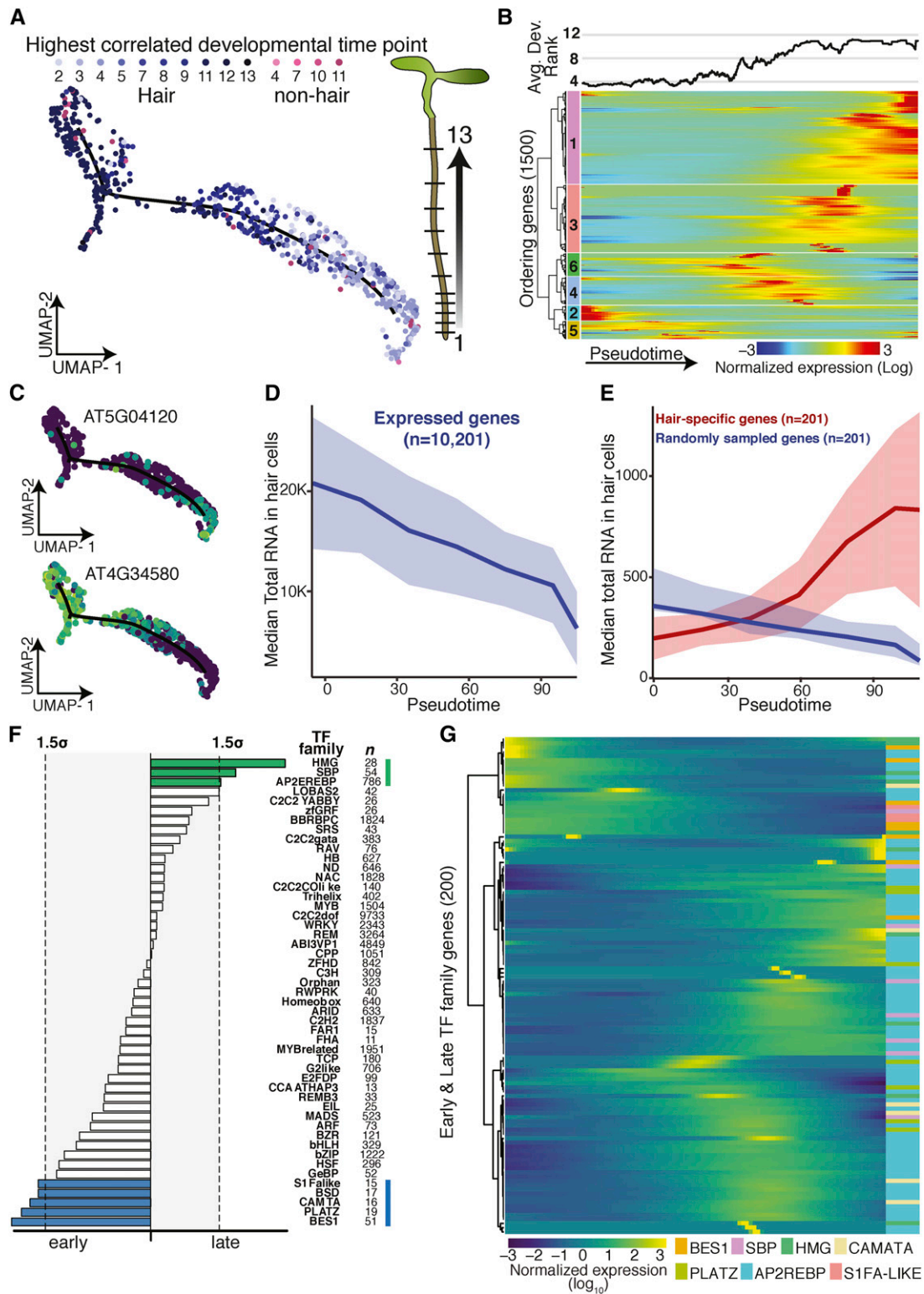


**Figure 4.** Developmental Trajectory of Hair Cells.

(A) UMAP-clustered hair cells were assigned a developmental time point based on highest Spearman’s rank correlation with bulk expression data of staged tissue (13 developmental stages; Brady et al., 2007; Cartwright et al., 2009). Cell type and developmental time points are indicated in shades of blue (and pink). Graphic illustrates developmental stages in Arabidopsis root (plant illustrations).

involved in lateral root formation and cell plate formation (Figure 6C; Van Damme et al., 2011). Louvain component 9 also showed a strong, but short branching point. We did not find any biological processes enriched in genes expressed specifically in this short branch; however, one gene whose expression is known to be affected by protoplasting was specifically expressed in these cells, perhaps reflecting that cells within this branch were more stressed by our experimental procedure (data not shown).

### Heat-Shocked Root Cells Show Subtle Expression Differences among Cell Types

A major question in studying plant responses to abiotic stress, such as heat or drought, is the extent to which such responses are nonuniform across cell types. Canonically, the heat stress response is characterized by rapid and massive upregulation of a few loci, mostly encoding heat-shock proteins, with dramatic downregulation of most other loci, in part because of altered mRNA splicing and transport (Yost and Lindquist, 1986, 1988; Saavedra et al., 1996). In plants, a set of 63 genes, most encoding heat-shock proteins, show extreme chromatin accessibility at both promoter and gene body upon heat stress, consistent with their high expression (Sullivan et al., 2014). In mammals and insects, not all cells are competent to exhibit the hallmarks of the heat-shock response (Dura, 1981; Morange et al., 1984); specifically, cells in early embryonic development fail to induce heat-shock protein expression upon stress.

We explored whether all cells within developing roots were capable of exhibiting a typical heat-shock response. To do so, we applied a standard heat stress (45 min, 38°C) to 8-d-old seedlings, harvested their roots along with roots from age- and time-matched control seedlings, and generated protoplasts for single cell RNA-Seq of both samples. For the control sample, we captured 1,076 cells, assaying expression for a median 4,079 genes per cell and a total of 22,971 genes; 82.7% of reads mapped to the TAIR10 genome assembly. The results for these control cells were similar to those described earlier with regard to captured cell types, proportion of cell types (e.g. 28.8% versus 34% annotated hair cells and 9.7% versus 7.2% endodermis cells), and correlation of gene expression ( $R^2 = 0.86$  for the 21,107 genes captured in both

experiments). For the heat-shock sample, we captured 1,009 cells, assaying expression for a median 4,384 genes per cell and a total of 21,237 genes; 79.8% of reads mapped to the TAIR10 genome assembly.

Due to global gene expression changes upon heat shock, we could not simply assign cell and tissue types as before for heat-shocked cells. The overwhelming impact of heat shock was also apparent when comparing the first and second highest cell-type and developmental Spearman's rank correlations for control cells and heat-shocked cells. Upon heat shock, many cells, especially those with nonhair, phloem, and columella as their highest rank, commonly showed as their second highest rank a different cell type instead of another developmental time point of the same cell type as observed in control cells (Supplemental Figure 11A). Unsurprisingly, the drastic changes in gene expression led to cells being embedded in UMAP space primarily as a function of treatment, making direct comparisons of treatment effects on any one cell type impossible (Supplemental Figure 11B). To enable such comparisons, we used a mutual nearest-neighbor to embed cells conditioned on treatment in UMAP space (Haghverdi et al., 2018). The mutual nearest-neighbor method was originally developed to account for batch effects by identifying the most similar cells between each batch and applying a correction to enable proper alignment of data sets. Here, we employ this technique to overcome the lack of marker expression in our heat-shock-treated cells and match them to their untreated counterpart based on overall transcriptome similarity (Figure 7A). This procedure yielded corresponding clusters in control and heat-shocked cells, albeit with varying cell numbers for most (Supplemental Figure 11C; Supplemental Table 2).

In response to stress, organisms are thought to upregulate stress genes and to specifically downregulate genes involved in growth and development to optimize resource allocation. In response to heat stress, this presumed "dichotomy" in gene expression is mirrored by the rapid localization of RNA polymerase II to the heat-shock gene loci and its depletion elsewhere in the genome (Teves and Henikoff, 2011). Our data provide strong evidence of this regulatory trade-off at the level of individual cells. Using hair cells (Louvain component 2) as an example, we found that hair-cell-specific genes are overwhelmingly repressed and

#### Figure 4. (continued).

**(B)** Cells were ordered in pseudotime; columns represent cells, rows represent expression of the 1,500 ordering genes. Rows were grouped based on similarity in gene expression, resulting in six clusters (indicated left), with genes in clusters 2 and 5 expressed early in pseudotime, and genes in cluster 1 expressed late. Hair cells with the earliest developmental signal (Brady et al., 2007; Cartwright et al., 2009) were designated as the root of the trajectory. The graph above represents the average best-correlation of developmental stage (Brady et al., 2007; Cartwright et al., 2009) in a scrolling window of 20 cells with pseudotime, showing the expected increase in developmental age with increasing pseudotime.

**(C)** Examples of an early and a late expressed hair-cell-specific gene. Gene expression in each cell is superimposed onto the UMAP cluster and trajectory, with lighter colors indicating higher gene expression.

**(D)** Median total RNA captured in cells decreases across pseudotime. Number of genes included is indicated.

**(E)** Comparison of median total RNA for hair-cell-specific genes (in red) to a comparable random set of genes (in blue). Number of genes is indicated (Permutation test  $P$  value  $\approx 10^{-4}$ ).

**(F)** Different transcription factor motifs reside in the 500-bp upstream regions of genes expressed early (clusters 2 and 5) compared with genes expressed late (cluster 1). Transcription factor motifs specific to early hair cells are denoted with blue bars, those for late hair cells with green bars; bar length indicates motif frequency. Thresholds on either side (gray box, dotted lines) refer to 1.5 SD above mean motif frequency.

**(G)** Expression of individual members of transcription factors families highlighted in **(D)** across pseudotime identifies candidate factors driving early or late gene expression.

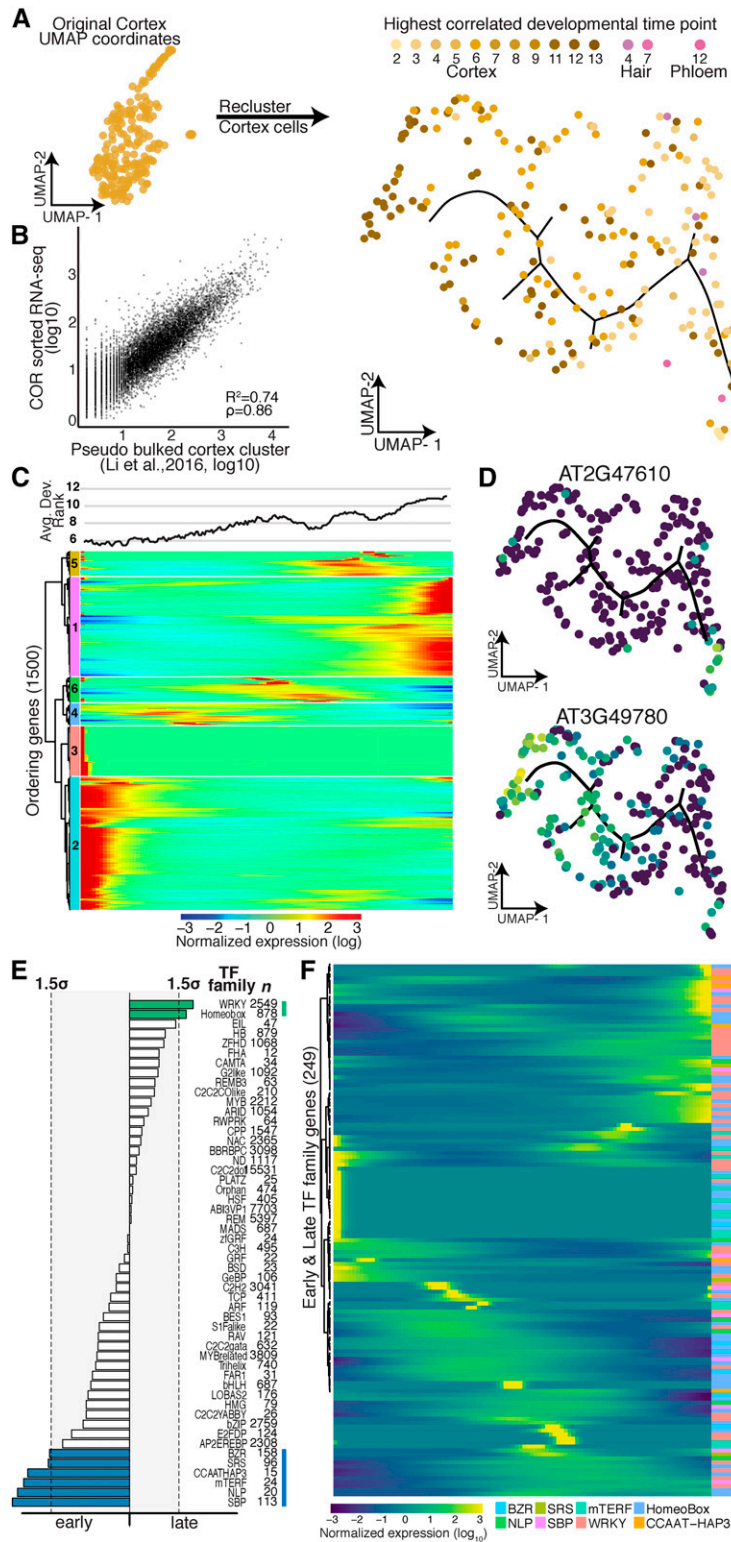


**Figure 5.** Developmental Trajectory of Cortex Cells.

**(A)** Cortex cells were reclustered to create a trajectory, in which each cell was assigned a developmental time point and identity (shades of yellow, brown, and pink) based on the highest Spearman’s rank correlation of a cell’s gene expression with prior sorted bulk data (Brady et al., 2007; Cartwright et al., 2009).

that heat-shock genes are upregulated, often dramatically so (Figures 7B and 7D). Indeed, *HEAT SHOCK PROTEIN 101* (*HSP101*), the most highly expressed and chromatin-accessible gene upon heat shock in previous studies (Sullivan et al., 2014), was strongly expressed across all clusters whereas expression of the hair marker gene *COBL9* decreased dramatically upon stress (Figures 7C and 7D).

Having established comparable clusters, we next identified genes that were differentially expressed as a function of treatment and cluster identity, excluding those with <15 cells in either control or heat-shock conditions. This analysis identified 8,526 genes (false discovery rate [*FDR*] < 0.1%) whose expression was altered by heat-shock treatment in one or more clusters; of these, 2,627 genes were up- or downregulated at least twofold (Figure 7E; Supplemental Data Set 5; *FDR* < 0.1% and absolute value of log<sub>2</sub>-fold change > 1). As for hair cells (Figure 7B), cell-type marker genes for all clusters were enriched among the downregulated genes upon heat shock. To identify cluster-specific differences in the response to heat shock, we compared gene expression of cells within individual clusters to the rest of the cells across treatments. We observed the largest number of cluster-specific gene expression changes in hair, nonhair, and cortex cells (Figure 7F). As these cell types are the three outermost cell layers of the root, they may be exposed more directly to the heat shock and respond more quickly. Genes differentially expressed in hair cells (Louvain component 2) upon heat shock were enriched for ribosome-associated genes and RNA methylation. Stele cells (Louvain component 6) showed differential expression of genes involved in cell wall organization and biogenesis, and endodermis cells (Louvain component 4) showed differential expression of genes involved in response to external, chemical, and stress stimuli as well as nitrate and anion transport (Figure 7F).

The expression of heat-shock proteins protects cells from heat shock and aids their recovery (Parsell et al., 1993; Parsell and Lindquist, 1993; Queitsch et al., 2000). We were interested in whether we could detect cluster- and cell-type-specific differences in the canonical heat-shock response. In principle, such differences could be exploited to alter heat-shock protein expression in a cell-type-specific manner to boost plant heat and drought tolerance without pleiotropically decreasing whole organism fitness. To address such possible differences, we focused

on genes that from bulk analyses have differential expression upon heat shock (1,783 genes) or reside near regulatory regions that change in accessibility upon heat shock (1,730 genes; Sullivan et al., 2014; Alexandre et al., 2018). Although these gene sets overlap (942 genes), they contain complementary information, as changes in accessibility do not necessarily translate into altered expression, and vice versa (Alexandre et al., 2018). In our single cell expression analysis, we identified 752 of 1,783 heat-responsive genes as differentially expressed upon heat shock, and 564 of 1,730 genes near dynamic regulatory regions as differentially expressed. We hierarchically clustered control and heat-shock-treated single cell transcriptomes for both gene sets (Supplemental Figures 12A and 12C), resulting in several gene clusters with distinct expression patterns. Overall, cellular responses were dominated by the canonical heat-shock response, as visualized in cluster 4 (Supplemental Figure 12A) and cluster 2 (Supplemental Figure 12C). The 63 genes showing extreme accessibility and high expression upon heat shock (Sullivan et al., 2014) are largely contained in these two clusters (Supplemental Figure 12A, cluster 4, 49 of 63; Supplemental Figure 12C, cluster 2, 42 of 63).

Our analysis also revealed subtle but significant differences among some tissue types (Supplemental Figures 12A and 12B, e.g. clusters 3 and 8; Supplemental Figures 12C and 12D, e.g. clusters 5 and 7; Supplemental Data Set 6). Although most of these gene clusters were not enriched for specific annotations, cluster-8 genes were associated with rRNA metabolic processes (*P* value = 0.048) and cluster-5 genes (Supplemental Figures 12A and 12B) were enriched for transport genes (*P* value = 0.045). These results demonstrate both the promise and the challenges inherent in comparing single cell data across different conditions and treatments.

## DISCUSSION

Here, we use *Arabidopsis* roots to establish both experimental and analytic procedures for single cell RNA-Seq in plants. Using Monocle 3, we could assign over 3,000 cells to expected cell and tissue types with high confidence. In particular, cortex, endodermis and hair cells were easily identified. However, distinguishing other cell types was challenging. For example, nonhair

**Figure 5.** (continued).

**(B)** Comparison of pseudo-bulk expression data from cells annotated as cortex cells with bulk expression data from protoplasts sorted for expression of the cortex marker gene *COR* (Li et al., 2016).

**(C)** Cells were ordered in pseudotime; columns indicate cells, and rows the expression, of the 1,500 ordering genes. Rows were grouped based on similarity in gene expression, resulting in six clusters (indicated left), with genes in clusters 2 and 3 expressed early in pseudotime and genes in cluster 1 expressed late. Cortex cells with the earliest developmental signal (Brady et al., 2007; Cartwright et al., 2009) were designated as the root of the trajectory. The graph above represents the average best-correlation of developmental stage (Brady et al., 2007; Cartwright et al., 2009) in a scrolling window of 20 cells with pseudotime, showing the expected increase in developmental age with increasing pseudotime.

**(D)** Examples of an early and a late expressed novel cortex-cell-specific gene. Gene expression in each cell is superimposed onto the UMAP cluster and trajectory, with lighter colors indicating higher gene expression.

**(E)** Different transcription factor motifs reside in the 500-bp upstream regions of genes expressed early (clusters 2 and 3) compared with genes expressed late (cluster 1). Transcription factor motifs specific to early cortex cells are denoted with blue bars, and those for late cortex cells with green bars; bar length = motif frequency. Thresholds on either side (gray box, dotted lines) refer to 1.5 sd above mean motif frequency.

**(F)** Expression of individual members of transcription factor families highlighted in **(D)** across pseudotime identifies candidate factors driving early or late gene expression.

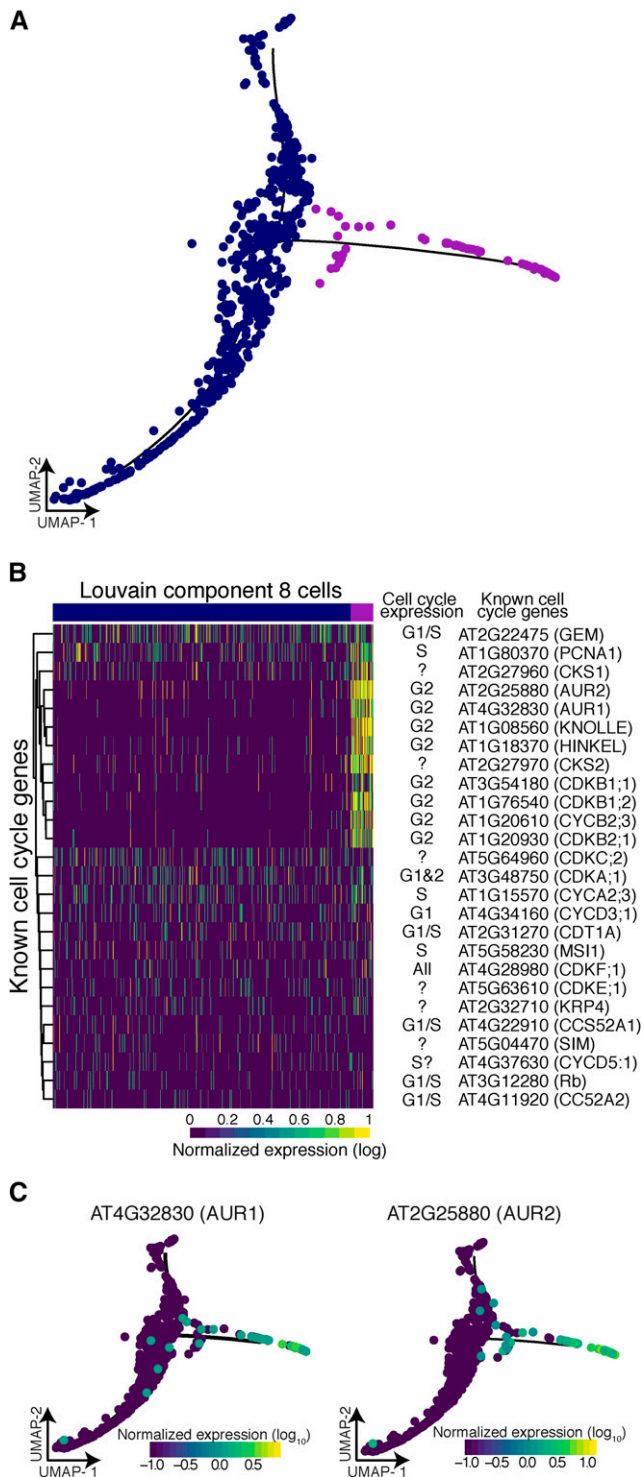


**Figure 6.** Branch Analysis Reveals Actively Dividing Cells.

**(A)** The 70 cells that resided in the branch of Louvain component 8 (purple) show significant branch-specific expression of genes enriched for cell-cycle function.

**(B)** Comparison of all known cell-cycle genes with expression in at least 5% of cells in Louvain component 8. Known cell-cycle expression is denoted for each gene, if unknown ‘?’.

and columella cells had high similarity in their expression profiles, consistent with their correlation in bulk expression data (Brady et al., 2007; Cartwright et al., 2009). Similarly, it was difficult to designate cells in Louvain component 8 as early nonhair cells, as these cells showed overlapping expression signatures for early nonhair cells, lateral root caps, and epidermis cells before differentiation to hair and nonhair cells. These Louvain component-8 cells were difficult to distinguish further with the sparse expression data typical for single cell analysis; however, we postulate that the root of the trajectory are cells dividing out of the epidermis/root cap precursor and these cells either become root cap cells or epidermis.

We also could not initially split stele tissue into individual cell types, likely because the difficulty of digesting the cell walls of the tightly packed vascular bundle resulted in fewer cells than expected (Brady et al., 2007; Cartwright et al., 2009). However, analyzing stele cells separately yielded six subclusters, which correspond to known vasculature cell types. Our approach to annotate these subclusters exemplifies the ad hoc nature of current single cell genomics studies, which require all available sources of information to be exploited to interpret the genomic data. Neither Spearman rank correlations with sorted bulk RNA-Seq data nor microarray expression data yielded obvious cluster identities. However, mean expression values of genes known to be expressed in vasculature cell types allowed us to assign the stele subclusters.

We identified hundreds of novel genes with cell-type-specific and tissue-type-specific expression, which may allow the generation of new marker lines for detailed genetic analyses. These genes, together with cluster-specific enriched transcription factor motifs and their corresponding transcription factors, are candidates for driving differentiation and cell-type identity. Similarly, the developmental trajectories we identified highlight the potential of single cell transcriptomics to advance a high-resolution view of plant development. These trajectories can be detected without the use of spatial information because plants have a continuous body plan with new cells continuously arising while older cells persist. Additionally, while this study allowed us to infer transcription factor motifs and candidate transcription factors, future analyses with greater numbers of cells than assayed here may include combinatorial expression of multiple transcription factor family members.

We explored the relationships of endoreduplication, transcriptional rates, and differentiation to find that transcriptional rates, measured as mRNA velocity, increase with increasing ploidy. However, this transcriptional increase appears to be limited to genes specifically expressed in hair cells, as overall levels of RNA decreased over pseudotime. These observations are consistent with hair cells becoming more specialized and moving toward a terminally differentiated state over time. However, this phenomenon of increasing specialization was not as apparent in other cell types. This difference may be due to biological causes,

**(C)** Two kinases, *AUR1* and *AUR2*, were specifically expressed in branch cells. These genes are involved in cell plate formation and lateral root formation.



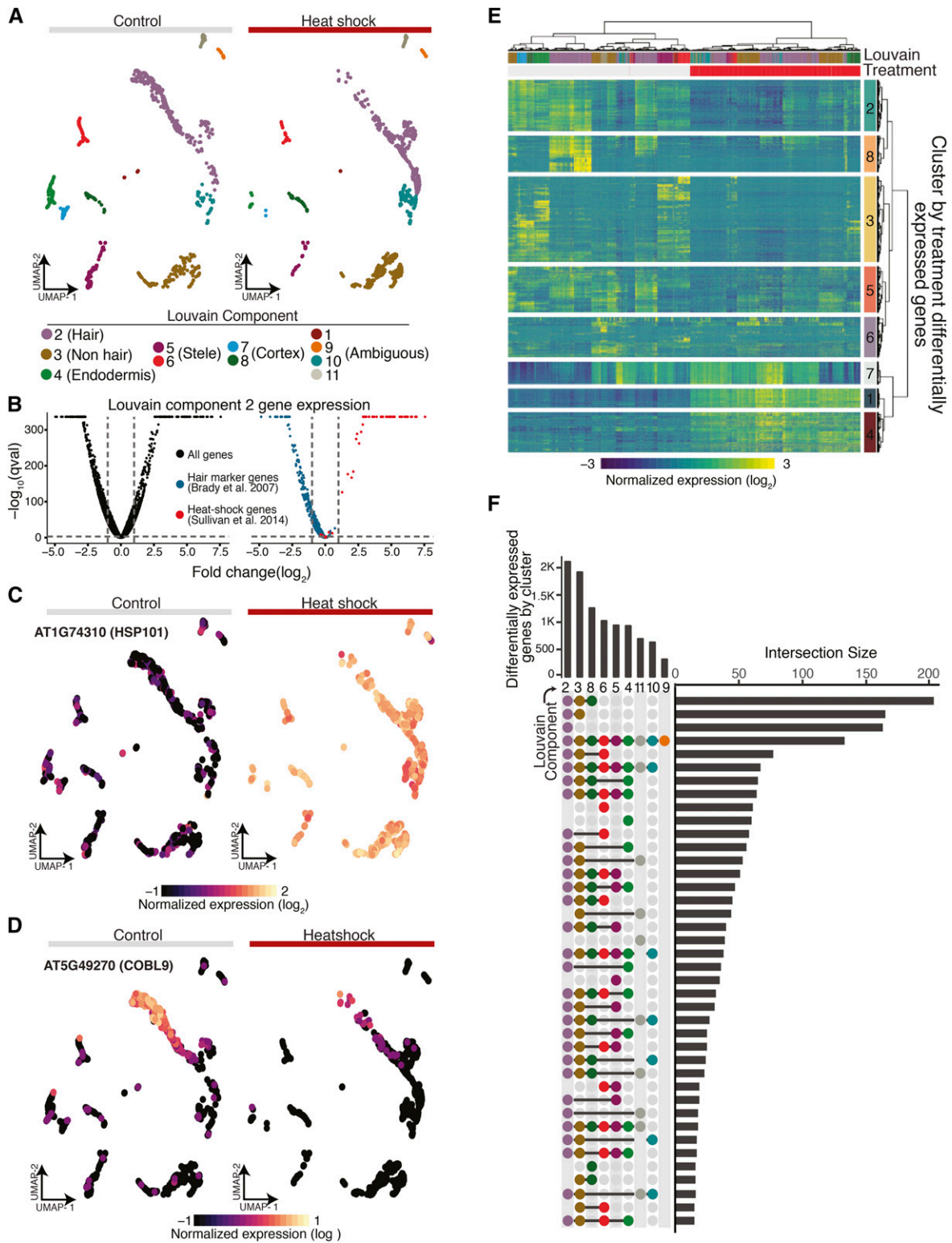


**Figure 7.** Single-Cell RNA-Seq Highlights Canonical and Novel Aspects of the Heat-Shock Response.

(A) A nearest-neighbor approach aligns control and heat-shocked cells in a UMAP embedding to allow for concomitant cluster/cell-type assignment. (B) Volcano plots of average gene expression change upon heat shock within Louvain component 2 for all genes (black), known hair marker genes (blue), and heat-shock signature genes (red).

such as the higher rates of endoreduplication in hair cells, or to technical causes, such as the better clustering and trajectory of hair cells compared with the other cell types assayed.

By allowing trajectories with side branches, we discovered that branch points can mark developmental decisions. In Louvain component 8, the small but distinct cell-cycle-enriched branch may mark lateral root primordia cells differentiating into epidermal cells or epidermal/lateral root precursor cells. Cells within this branch express many cell-cycle genes, among them members of the *CDK B* family that govern the G2 to M transition. Moreover, these cells specifically express the *AUR1* and *AUR2* genes, which function in cell plate formation; plants with mutations in these genes lack lateral roots (Van Damme et al., 2011). Although expression of cell-cycle genes may persist in nondividing cells because of their roles in endoreduplication, *AUR1* and *AUR2* expression (and cell plate formation) should not persist, consistent with our speculation that the cells within this branch are actively dividing cells in the G2 to M transition (Gutierrez, 2009). We also examined the cells in Louvain component 1 (designated endodermis) that are nearer to Louvain component 10 (designated cortex). The cells residing in this position correlate best with cortex endodermis initial cells.

We explored the Arabidopsis heat-shock response with single cell RNA-Seq because not all cells and tissues are equally competent to respond to stress. By identifying plant cell types that most strongly respond to abiotic stresses such as heat, drought, and nutrient starvation, ultimately we may be able to genetically manipulate relevant cell types to generate stress-tolerant crops without pleiotropically affecting plant fitness and yield. Although all heat-shocked cells showed gene expression changes typical of the canonical heat-shock genes, we detected subtle but highly significant expression differences among cells and tissue types for other genes. Thus, single cell transcriptomics across stress conditions holds potential for future crop breeding and genetic engineering. However, such analyses require much larger numbers of cells than currently accessible by droplet-based methods. Moreover, such analyses should focus on treatments that are less overwhelmed by a strong canonical signal to increase resolution in detecting cell-type-specific differences.

In this study, we relied on the extensive and detailed expression data for bulk Arabidopsis cell and tissue types to establish the validity of our approaches. The overwhelming correspondence of our findings with these and other data derived from traditional molecular genetics provides confidence that less well-characterized Arabidopsis tissues and other plants, including crops, will be amenable to these approaches. Thus, continued progress on single cell RNA-Seq experiments should have a major

impact on the analysis of plant development and environmental response.

## METHODS

### Plant Material and Growth Conditions

Arabidopsis (*Arabidopsis thaliana*) Col-0 seedlings were grown vertically at 22°C, on 1× Murashige and Skoog (MS) + 1% Suc (w/v) plates covered with one layer of filter paper. Seven- or 8-d-old seedlings (Long Day, 16-h light/8-h dark, ~100 μmol m<sup>-2</sup> s, 50% relative humidity) were collected around Zeitgeber Time 3, and the roots/shoots excised with a sharp razor blade. For the heat shock, seedling plates were transferred from 22°C to 38°C for 45 min (Conviron TC-26, ~100 μmol m<sup>-2</sup> s, 4100 K, 82 CRI, Sylvania Octron F017/84/Eco fluorescence bulbs), and the roots harvested immediately after.

### Protoplast Isolation

Protoplast isolation was done as described in Bargmann and Birnbaum (2010), with slight modifications. Briefly, 1 g of whole-roots was incubated in 10 mL of protoplasting solution for 1.5 h at 75 rpm. After passing through a 40-μm strainer, protoplasts were centrifuged at 500 g for 5 min and washed once in protoplasting solution without enzymes. Final suspension volume was adjusted to a density of 500 to 1,000 cells/μL. Protoplasts were placed on ice until further processing.

### Single-Cell RNA-Seq Protocol

On two separate sets of Arabidopsis root protoplasts on separate days, single cell RNA-Seq was performed using the 10× scRNA-Seq platform, the Chromium Single Cell Gene Expression Solution (10× Genomics).

### Data Analysis

#### Estimating Gene Expression in Individual Cells

Single cell RNA-Seq reads were sequenced and then mapped to the TAIR10 Arabidopsis genome using the software Cellranger (v. 2.1.0; <https://support.10xgenomics.com/single-cell-gene-expression/software/pipelines/latest/what-is-cell-ranger>). Cellranger produces a matrix of UMI counts where each row is a gene and each column represents a cell. The ARAPORT gene annotation was used. For the heat-shock analysis, reads from a control sample and reads from a heat-shocked sample were aggregated using “cellranger aggr” to normalize libraries to an equivalent number of mean reads per cell across libraries.

#### Running Monocle 3: Dimensionality Reduction, and Cell Clustering

The output of the Cellranger pipeline was parsed into R (v. 3.5.0) using the Cellranger R kit (v. 2.0.0) and converted into a CellDataSet (CDS) for further analysis using the software Monocle 3 Alpha (v. 2.99.1; <http://cole-trapnell-lab.github.io/monocle-release/monocle3/>). All Monocle 3 analysis was

**Figure 7.** (continued).

**(C)** *HSP101*, a signature heat-shock gene, shows dramatic increase of expression in all cell types upon heat shock.

**(D)** *COBL9*, a well-studied hair marker gene, is strongly repressed upon heat shock.

**(E)** Heat map of differentially expressed genes upon heat shock (top red bar; control, top gray bar), hierarchically clustered by both cells and genes (*FDR* < 0.1% and absolute value of the log<sub>2</sub> fold change > 1).

**(F)** “Upset” plot (Lex et al., 2014) of the number of differentially expressed genes as a function of heat shock for each Louvain cluster in our UMAP embedding (bars on top) along with the number of the intersect of differentially expressed genes between Louvain clusters (bars on the right). A surprising number of differentially expressed genes were specific to certain clusters (single dot in vertical row of dots).

performed on a High Performance Computing cluster using 128 GB of RAM spread across eight cores. The lower detection limit for the CDS was set at 0.5, and the expression family used set to `negbinomial.size()`.

We visualized cell clusters and trajectories using the standard Monocle workflow. Monocle internally handles all normalization needed for dimensionality reduction, visualization, and differential expression via size factors that control for variability in library construction efficiency across cells. After estimating the library size factors for each cell (via `estimateSizeFactors`) and estimating the dispersion in expression for each gene (via `estimateDispersions`) in the data set, the top 1,500 genes in terms of dispersion, i.e. 1,500 genes with the most expression variability in our data set, were selected to order the cells into clusters. The expression values of these 1,500 genes for each cell were log-transformed and projected onto the first 25 PCs via Monocle's data pre-processing function (`preprocessCDS`). Then, these lower-dimensional coordinates were used to initialize a nonlinear manifold learning algorithm implemented in Monocle 3 called "UMAP" (via `reduceDimension`; McInnes et al., 2018). This allows us to visualize the data into two or three dimensions. Specifically, we projected onto two components using the "cosine distance" metric, setting the parameters `n_neighbors = 50`, and `min_dist = 0.1`.

The Louvain method was used to detect cell clusters in our two-dimensional representation of the data set (`partitionCells`); this resulted in 11 cell clusters, or Louvain components. Cells were then clustered into super groups using a method derived from approximate graph abstraction (Wolf et al., 2018) and for each super group, a cell trajectory was drawn atop the projection using Monocle's reversed graph embedding algorithm, which is derived from SimplePPT (`learnGraph`; Mao et al., 2015). This yielded six cell trajectories.

To further analyze the clusters we annotated as stele, clusters 3, 4, and 7 were reclustered together and were reanalyzed using Monocle 3 as previously described in this article except the parameter "min\_dist" was changed to "0.05" when the "reduceDimension function" was called. This revealed six additional subclusters.

To further analyze the cluster we annotated as cortex, Cluster 10 was reclustered and reanalyzed using Monocle 3 as previously described in this article except the parameters "n\_neighbors" was reduced to 25. This did not reveal any subclusters, but a trajectory was generated.

### Estimating Doublets

Single Cell Remover of Doublets (Scrublet) was used to predict doublets in our scRNA-Seq data (<https://github.com/AllonKleinLab/scrublet>). Using the software Python 3.5, Scrublet was run using default settings as described by the example tutorial that is available as a Python notebook ([https://github.com/AllonKleinLab/scrublet/blob/master/examples/scrublet\\_basics.ipynb](https://github.com/AllonKleinLab/scrublet/blob/master/examples/scrublet_basics.ipynb)). The only significant change was that expected double rate was set to 0.1; in the tutorial it is 0.06.

### Identifying Cell Types

To categorize the cells into cell types and to apply developmental information, a deconvolved root expression map was downloaded from The Arabidopsis Gene Expression Database (AREX LITE; <http://www.aredb.org/data/decondatamatrix.zip>). Using this data matrix, the Spearman's rank correlation was calculated between each cell in our data set and each cell type and longitudinal annotation in the data matrix ( $3,121 \times 128$  Spearman's rank correlations total). Specifically, we looked at the correlation of 1,229 highly variable genes in our data set. These 1,229 genes represent the overlap between our 1,500 highly variable genes and genes in the root expression map data matrix. Cells in our data set were assigned a cell type and a developmental label based on the annotation with which each cell had the highest correlation (i.e. if a cell correlated highest with the endodermis cells in longitudinal zone 11, then it would be called as `endodermis_11`).

In addition to using the Spearman's rank correlation to assign cells their cell type, a set of known marker genes derived from green fluorescent

protein (GFP) marker lines of the Arabidopsis root were used to identify cell types based on the high gene expression of these marker genes. These genes were obtained from Brady et al. (2007) and Cartwright et al. (2009). Specifically, Supplemental Table 2 from Cartwright et al. (2009) was used. For the analysis comparing bulk RNA and pseudo bulk scRNA-Seq data, the bulk data were obtained from Li et al. (2016); specifically, we used Supplemental Table 5 from that study. Isoforms of each gene were averaged, to be comparable to the pseudo bulk data. Lastly, using this same bulk RNA-Seq data, the Pearson correlation was calculated between each cell in our data set and each GFP marker line. Cells in our data set were assigned to a GFP marker line based on the GFP marker line with which each cell had the highest correlation.

### Running Monocle 3: Identifying High-Specificity Genes

To identify differentially expressed genes between cell clusters, the Moran's I test was performed on our UMAP (`principalGraphTest`), with the projection being broken up into  $25 \times 25$  spatial units. Then marker genes were identified for each cluster, and each annotated grouping of clusters using a Moran's I threshold of 0.1 and a  $q_{val}$  threshold of 0.05. For a gene to be considered highly specific, it must have had a specificity rating of  $>0.7$ .

### Transcription Factor Motif Analysis

Highly specific genes were identified for each cell cluster, and their promoters were analyzed for presence of transcription factor motifs. Promoters were defined as 500 bp upstream of the start site of each gene. Instances of each motif were identified using the method from Grant et al. (2011) at a  $P$  value cutoff of  $1e-5$  for each match. The input position weight matrices for each motif were enumerated in a previous study of binding preferences for nearly all Arabidopsis transcription factors (O'Malley et al., 2016). Motif frequencies in genes specific to each cell cluster were compared with a background set of motif frequencies across all promoters in the Arabidopsis genome to determine a log<sub>2</sub> enrichment score. Transcription factor family genes were pulled from the gene family page of TAIR10 (<https://www.arabidopsis.org/browse/genefamily/index.jsp>).

### Running Monocle 3: Assigning Pseudotime

Pseudotime analysis requires the selection of a cell as an origin for the pseudotime trajectory. Origin assignment was based on the Spearman's rank assignments for each cell. The following cells were used as origins for their respective cell-type trajectories: `cortex_2`, `hair_2`, `endodermis_2`, `nonHair_3`. The `get_correct_root_state()` function was used to assign the root of a trajectory, and the `orderCells()` function was used to assign cells a pseudotime value.

### Calculating Total mRNA

After pseudotime analysis was performed on a cell cluster, cells were binned together such that each bin contained a similar number of cells and each bin represented cells from similar pseudotimes. The median total mRNA and the  $sd$  of the total mRNA of each bin was then calculated.

### Calculating Significance with the Permutation Test

The permutation test was used to calculate the significance of observed trends that the total mRNA of hair marker genes and hair-specific genes increased as pseudotime increased in hair cells. To do this, 10,000 random samplings of 441 genes (the number of hair marker genes) and 201 genes (the number of hair specific genes) were taken respectively. Next, the median total mRNA was calculated across pseudotime for each random sampling and the slope of this data was calculated using a generalized linear model. The observed slope of the marker genes and the hair-specific genes was compared with the distribution of slopes generated by 10,000

random samplings. No random sampling of genes had a slope that was higher than the observed slopes generated by the hair marker genes or the hair-specific genes. The significance, or the  $P$  value, of the trend seen in the hair marker genes and the hair-specific genes can then be calculated simply as the proportion of sampled permutations that have a slope that is equal to or greater than the slope generated by our genes of interest. This gives us a  $P$  value =  $1/10,001$ , or roughly  $10^{-4}$ .

### Analyzing Expression Differences between Branches of Louvain Component 8 (Early Nonhair)

To identify genes responsible for the branching in the pseudotime trajectory of Louvain component 8 (early nonhair), the principal graph test was used to identify genes with expression specific to the side branch versus the main branch. Genes were considered specific if they had a specificity value  $>0.8$ . Genes were removed from the analysis if they did not have expression in at least 10% of the cells considered and a mean expression  $>0.25$ .

### Calculating RNA Velocity

We used the Velocity R and Python packages (v. 0.6 and 0.17, respectively) to estimate RNA velocity for root hair cells (La Manno et al., 2018). Matrices of spliced and unspliced RNA counts were generated from Cell Ranger outputs using velocity.py CLI and run 10x defaults. We followed the velocity.py and velocity.R manuals (<http://velocity.org/>) and used spliced (emat) and unspliced (nmat) matrices to estimate RNA velocity. With predefined cell-type annotations, we performed gene filtering with the parameter min.max.cluster.average set to 0.2 and 0.05 for emat and nmat respectively. RNA velocity using the selected 996 genes was estimated with the defaults to the function gene.relative.velocity.estimates() except parameters kCells and fit.quantile which were set to 5 and 0.05, respectively. Velocity measurements for each cell were calculated as the difference between \$projected and \$current (with \$deltaT = 1) results from the estimated velocity output.

### Analysis of Heat-Shock Data

For each pair of cell types and for each gene cluster, we used a generalized linear model to determine the significance of an interaction between the effects of cell type and heat treatment on the normalized expression level of genes in that cluster. Then, to identify differentially expressed genes specific for every Louvain cluster, we subsetted cells from every cluster that contained 15 or more cells in both control and treated conditions, estimated dispersions for each subset, and tested for differential gene expression identified using the differentialGeneTest function in Monocle specifying a full model of Treatment cluster and a residual model of 1.  $FDR$  values per gene were then obtained across all tests using the Benjamini-Hochberg method. The overlap of differentially expressed genes as a function of heat-shock treatment between clusters was visualized using an UpsetR plot. Briefly, a binary matrix of differentially expressed genes by cluster was generated where gene-cluster combinations were set to 1 (significant) or 0 (not significant). This matrix was then passed to the upset function from the UpsetR R package specifying nine sets and ordering by frequency. To identify whether clusters contained subtle differences in the expression of previously identified heat-shock-responsive genes, we tested for differential gene expression across all cells and clusters and identified the intersect between differentially expressed genes obtained from single cell profiles and previously identified dynamic changes in DNase I Hypersensitive Sites (DHSs)-linked genes and bulk-differentially expressed genes upon heat shock. Differentially expressed genes as a function of heat-shock treatment for all cells in unison were identified using the differentialGeneTest function in Monocle, specifying a full model of Treatment\*UMAP cluster and a residual model of UMAP cluster. Hierarchical clustering of these DHS-linked and bulk-differentially expressed gene sets across control and heat-shock-treated cells was performed using the

heatmap function in the heatmap R package (v. 1.0.10) specifying ward.D2 as the clustering method. Genes with similar dynamics across treatment and cell types were recovered using the cutree function from the “stats” package in R, specifying  $k = 8$  for both DHS-linked genes and bulk differentially expressed genes. To generate signatures from these eight groups of clustered genes, we log-normalized expression values using a pseudocount of 1, and for each cell calculated the mean normalized expression value across genes that belong to one of the eight gene clusters.

### Accession Numbers

All sequencing data can be found on Gene Expression Omnibus at: <https://www.ncbi.nlm.nih.gov/geo/query/acc.cgi?acc=GSE121619>.

### Supplemental Data

**Supplemental Figure 1.** General tissue and data features.

**Supplemental Figure 2.** Pearson correlation to sorted RNA-seq samples.

**Supplemental Figure 3.** Marker gene expression in cell-type clusters.

**Supplemental Figure 4.** Examples of tissue-specific gene expression.

**Supplemental Figure 5.** Transcription factor family expression patterns.

**Supplemental Figure 6.** Spearman's rank correlation for each cell's development and tissue type.

**Supplemental Figure 7.** Changes in transcription across hair cell development.

**Supplemental Figure 8.** Developmental trajectory of endodermal cells.

**Supplemental Figure 9.** Median total RNA in cortex across pseudotime.

**Supplemental Figure 10.** Developmental expression of individual transcription factors.

**Supplemental Figure 11.** Heat-shock clustering and expression profiling.

**Supplemental Figure 12.** Conditional expression in genes with dynamic chromatin accessibility during heat shock.

**Supplemental Table 1.** Bulk RNA-seq comparisons to single cell RNA-seq.

**Supplemental Table 2.** Number of cells in the control-versus-heat-shock analysis.

**Supplemental Data Set 1.** List of ordering/high-dispersion genes.

**Supplemental Data Set 2.** Correlation with bulk expression data.

**Supplemental Data Set 3.** Marker genes.

**Supplemental Data Set 4.** Novel high-specificity genes.

**Supplemental Data Set 5.** Cluster-specific heat-shock differentially expressed genes.

**Supplemental Data Set 6.** Generalized linear model pairwise test of significance among cortex, hair, and nonhair cells.

### ACKNOWLEDGMENTS

We thank members of the Trapnell Lab for input and discussion. This work was supported by the National Science Foundation (NSF grant MCB-1516701 to C.Q., and NSF grant RESEARCH-PGR 1748843 to C.Q. and

S.F.); the University of Washington National Institutes of Health (Big Data for Genomics and Neuroscience Training Grant T32LM012419 to K.J.-B.); the National Institutes of Health (NIH grants U54DK107979, DP2HD088158, RC2DK114777, and R01HL118342 to C.T.); and the Paul G. Allen Frontiers Group (to C.T.).

#### AUTHOR CONTRIBUTIONS

J.T.C., C.M.A., and K.J.-B. performed and designed most of the experiments; K.J.-B. did most of the bioinformatic analysis; M.W.D. performed transcription factor enrichment analysis; L.S. performed RNA velocity analysis; J.L.M.-F. performed the heat-shock analysis; K.L.B. performed statistical analysis of heat-shock experiments; J.T.C., C.Q., and K.J.-B. wrote the majority of the article; C.T. and S.F. provided technical help and critical comments on this project.

Received October 31, 2018; revised February 12, 2019; accepted March 26, 2019; published March 28, 2019.

#### REFERENCES

- Alexandre, C.M., et al.** (2018) Complex relationships between chromatin accessibility, sequence divergence, and gene expression in *Arabidopsis thaliana*. *Mol. Biol. Evol.* **35**: 837–854.
- Bargmann, B.O.R., and Birnbaum, K.D.** (2010). Fluorescence activated cell sorting of plant protoplasts. *J. Vis. Exp.* **36**: 1673.
- Bennett, T., van den Toorn, A., Sanchez-Perez, G.F., Campilho, A., Willemssen, V., Snel, B., and Scheres, B.** (2010). SOMBRERO, BEARSKIN1, and BEARSKIN2 regulate root cap maturation in *Arabidopsis*. *Plant Cell* **22**: 640–654.
- Bhosale, R., et al.** (2018) A spatiotemporal DNA endploidy map of the *Arabidopsis* root reveals roles for the endocycle in root development and stress adaptation. *Plant Cell* **30**: 2330–2351.
- Birnbaum, K., Shasha, D.E., Wang, J.Y., Jung, J.W., Lambert, G.M., Galbraith, D.W., and Benfey, P.N.** (2003). A gene expression map of the *Arabidopsis* root. *Science* **302**: 1956–1960.
- Blondel, V.D., Guillaume, J.-L., Lambiotte, R., and Lefebvre, E.** (2008). Fast unfolding of communities in large networks. *J. Stat. Mech.* **2008**: 1–12.
- Bourdon, M., Pirrello, J., Cheniclet, C., Coriton, O., Bourge, M., Brown, S., Moïse, A., Peypelut, M., Rouyère, V., Renaudin, J.P., Chevalier, C., and Frangne, N.** (2012). Evidence for karyoplasmic homeostasis during endoreduplication and a ploidy-dependent increase in gene transcription during tomato fruit growth. *Development* **139**: 3817–3826.
- Brady, S.M., Orlando, D.A., Lee, J.Y., Wang, J.Y., Koch, J., Dinneny, J.R., Mace, D., Ohler, U., and Benfey, P.N.** (2007). A high-resolution root spatiotemporal map reveals dominant expression patterns. *Science* **318**: 801–806.
- Brennecke, P., Anders, S., Kim, J.K., Kołodziejczyk, A.A., Zhang, X., Proserpio, V., Baying, B., Benes, V., Teichmann, S.A., Marioni, J.C., and Heisler, M.G.** (2013). Accounting for technical noise in single-cell RNA-seq experiments. *Nat. Methods* **10**: 1093–1095.
- Cao, J., et al.** (2017) Comprehensive single-cell transcriptional profiling of a multicellular organism. *Science* **357**: 661–667.
- Cartwright, D.A., Brady, S.M., Orlando, D.A., Sturmfels, B., and Benfey, P.N.** (2009). Reconstructing spatiotemporal gene expression data from partial observations. *Bioinformatics* **25**: 2581–2587.
- Denyer, T., Ma, X., Klesen, S., Scacchi, E., Nieselt, K., and Timmermans, M.C.P.** (2019). Spatiotemporal developmental trajectories in the *Arabidopsis* root revealed using high-throughput single-cell RNA sequencing. *Dev. Cell* **48**: 840–852.
- Dura, J.M.** (1981). Stage dependent synthesis of heat shock induced proteins in early embryos of *Drosophila melanogaster*. *Mol. Gen. Genet.* **184**: 381–385.
- Efroni, I., Ip, P.-L., Nawy, T., Mello, A., and Birnbaum, K.D.** (2015). Quantification of cell identity from single-cell gene expression profiles. *Genome Biol.* **16**: 9.
- Efroni, I., Mello, A., Nawy, T., Ip, P.-L., Rahni, R., DeRose, N., Powers, A., Satija, R., and Birnbaum, K.D.** (2016). Root regeneration triggers an embryo-like sequence guided by hormonal interactions. *Cell* **165**: 1721–1733.
- Grant, C.E., Bailey, T.L., and Noble, W.S.** (2011). FIMO: Scanning for occurrences of a given motif. *Bioinformatics* **27**: 1017–1018.
- Gutierrez, C.** (2009). The *Arabidopsis* cell division cycle. *Arabidopsis Book* **7**: e0120.
- Haghverdi, L., Lun, A.T.L., Morgan, M.D., and Marioni, J.C.** (2018). Batch effects in single-cell RNA-sequencing data are corrected by matching mutual nearest neighbors. *Nat. Biotechnol.* **36**: 421–427.
- Irish, V.F.** (1991). Cell lineage in plant development. *Curr. Opin. Cell Biol.* **3**: 983–987.
- Katayama, H., Iwamoto, K., Kariya, Y., Asakawa, T., Kan, T., Fukuda, H., and Ohashi-Ito, K.** (2015). A negative feedback loop controlling bHLH complexes is involved in vascular cell division and differentiation in the root apical meristem. *Curr. Biol.* **25**: 3144–3150.
- Kieffer, M., Master, V., Waites, R., and Davies, B.** (2011). TCP14 and TCP15 affect internode length and leaf shape in *Arabidopsis*. *Plant J.* **68**: 147–158.
- Lachowiec, J., Lemus, T., Thomas, J.H., Murphy, P.J., Nemhauser, J.L., and Queitsch, C.** (2013). The protein chaperone HSP90 can facilitate the divergence of gene duplicates. *Genetics* **193**: 1269–1277.
- Lachowiec, J., Mason, G.A., Schultz, K., and Queitsch, C.** (2018). Redundancy, feedback, and robustness in the *Arabidopsis thaliana* BZR/BEH gene family. *bioRxiv* 053447; .
- La Manno, et al.** (2018) RNA velocity of single cells. *Nature* **560**: 494–498.
- Lan, X., and Pritchard, J.K.** (2016). Coregulation of tandem duplicate genes slows evolution of subfunctionalization in mammals. *Science* **352**: 1009–1013.
- Lee, C., Teng, Q., Zhong, R., and Ye, Z.H.** (2012). *Arabidopsis* GUX proteins are glucuronyltransferases responsible for the addition of glucuronic acid side chains onto xylan. *Plant Cell Physiol.* **53**: 1204–1216.
- Lex, A., Gehlenborg, N., Strobelt, H., Vuillemot, R., and Pfister, H.** (2014). UpSet: Visualization of intersecting sets. *IEEE Trans. Vis. Comput. Graph.* **20**: 1983–1992.
- Li, S., Yamada, M., Han, X., Ohler, U., and Benfey, P.N.** (2016). High-resolution expression map of the *Arabidopsis* root reveals alternative splicing and lincRNA regulation. *Dev. Cell* **39**: 508–522.
- Lucero, L.E., Uberti-Manassero, N.G., Arce, A.L., Colombatti, F., Alemanno, S.G., and Gonzalez, D.H.** (2015). TCP15 modulates cytokinin and auxin responses during gynoecium development in *Arabidopsis*. *Plant J.* **84**: 267–282.
- Mao, Q., Yang, L., Wang, L., Goodison, S., and Sun, Y.** (2015). SimplePPT: A simple principal tree algorithm. *In Proceedings of the 2015 SIAM International Conference on Data Mining*, pp. 792–800.
- McInnes, L., Healy, J., and Melville, J.** (2018). UMAP: Uniform Manifold Approximation and Projection for dimension reduction. *arXiv:1802.03426 [stat.ML]*. <https://arxiv.org/abs/1802.03426> .



- Morange, M., Diu, A., Bensaude, O., and Babinet, C.** (1984). Altered expression of heat shock proteins in embryonal carcinoma and mouse early embryonic cells. *Mol. Cell. Biol.* **4**: 730–735.
- Mortimer, J.C., Miles, G.P., Brown, D.M., Zhang, Z., Segura, M.P., Weimar, T., Yu, X., Seffen, K.A., Stephens, E., Turner, S.R., and Dupree, P.** (2010). Absence of branches from xylan in *Arabidopsis gux* mutants reveals potential for simplification of lignocellulosic biomass. *Proc. Natl. Acad. Sci. USA* **107**: 17409–17414.
- O'Malley, R.C., Huang, S.C., Song, L., Lewsey, M.G., Bartlett, A., Nery, J.R., Galli, M., Gallavotti, A., and Ecker, J.R.** (2016). Cis-trome and epicistrome features shape the regulatory DNA landscape. *Cell* **165**: 1280–1292.
- Ohashi-Ito, K., Saegusa, M., Iwamoto, K., Oda, Y., Katayama, H., Kojima, M., Sakakibara, H., and Fukuda, H.** (2014). A bHLH complex activates vascular cell division via cytokinin action in root apical meristem. *Curr. Biol.* **24**: 2053–2058.
- Packer, J., and Trapnell, C.** (2018). Single-cell multi-omics: An engine for new quantitative models of gene regulation. *Trends Genet.* **34**: 653–665.
- Parsell, D.A., and Lindquist, S.** (1993). The function of heat-shock proteins in stress tolerance: degradation and reactivation of damaged proteins. *Annu. Rev. Genet.* **27**: 437–496.
- Parsell, D.A., Taulien, J., and Lindquist, S.** (1993). The role of heat-shock proteins in thermotolerance. *Philos. Trans. R. Soc. London. Ser. B Biol. Sci.* **339**: 279–286.
- Peng, Y., Chen, L., Lu, Y., Wu, Y., Dumenil, J., Zhu, Z., Bevan, M.W., and Li, Y.** (2015). The ubiquitin receptors DA1, DAR1, and DAR2 redundantly regulate endoreduplication by modulating the stability of TCP14/15 in *Arabidopsis*. *Plant Cell* **27**: 649–662.
- Petricka, J.J., Winter, C.M., and Benfey, P.N.** (2012). Control of *Arabidopsis* root development. *Annu. Rev. Plant Biol.* **63**: 563–590.
- Qiu, X., Hill, A., Packer, J., Lin, D., Ma, Y.A., and Trapnell, C.** (2017a). Single-cell mRNA quantification and differential analysis with Census. *Nat. Methods* **14**: 309–315.
- Qiu, X., Mao, Q., Tang, Y., Wang, L., Chawla, R., Pliner, H.A., and Trapnell, C.** (2017b). Reversed graph embedding resolves complex single-cell trajectories. *Nat. Methods* **14**: 979–982.
- Queitsch, C., Hong, S.W., Vierling, E., and Lindquist, S.** (2000). Heat shock protein 101 plays a crucial role in thermotolerance in *Arabidopsis*. *Plant Cell* **12**: 479–492.
- Resentini, F., Felipo-Benavent, A., Colombo, L., Blázquez, M.A., Alabadi, D., and Masiero, S.** (2015). TCP14 and TCP15 mediate the promotion of seed germination by gibberellins in *Arabidopsis thaliana*. *Mol. Plant* **8**: 482–485.
- Riechmann, J.L., et al.** (2000) *Arabidopsis* transcription factors: Genome-wide comparative analysis among eukaryotes. *Science* **290**: 2105–2110.
- Rogers, E.D., and Benfey, P.N.** (2015). Regulation of plant root system architecture: Implications for crop advancement. *Curr. Opin. Biotechnol.* **32**: 93–98.
- Russell, A.B., Trapnell, C., and Bloom, J.D.** (2018). Extreme heterogeneity of influenza virus infection in single cells. *eLife* **7**: e32303.
- Ryu, K.H., Huang, L., Kang, H.M., and Schiefelbein, J.** (2019). Single-cell RNA sequencing resolves molecular relationships among individual plant cells. *Plant Physiol.* **179**: 1444–1456.
- Saavedra, C., Tung, K.S., Amberg, D.C., Hopper, A.K., and Cole, C.N.** (1996). Regulation of mRNA export in response to stress in *Saccharomyces cerevisiae*. *Genes Dev.* **10**: 1608–1620.
- Sullivan, A.M., et al.** (2014) Mapping and dynamics of regulatory DNA and transcription factor networks in *A. thaliana*. *Cell Reports* **8**: 2015–2030.
- Tan, T.T., Endo, H., Sano, R., Kurata, T., Yamaguchi, M., Ohtani, M., and Demura, T.** (2018). Transcription factors VND1–VND3 contribute to cotyledon xylem vessel formation. *Plant Physiol.* **176**: 773–789.
- Tatematsu, K., Nakabayashi, K., Kamiya, Y., and Nambara, E.** (2008). Transcription factor AtTCP14 regulates embryonic growth potential during seed germination in *Arabidopsis thaliana*. *Plant J.* **53**: 42–52.
- Teves, S.S., and Henikoff, S.** (2011). Heat shock reduces stalled RNA polymerase II and nucleosome turnover genome-wide. *Genes Dev.* **25**: 2387–2397.
- Trapnell, C.** (2015). Defining cell types and states with single-cell genomics. *Genome Res.* **25**: 1491–1498.
- Trapnell, C., Cacchiarelli, D., Grimsby, J., Pokharel, P., Li, S., Morse, M., Lennon, N.J., Livak, K.J., Mikkelsen, T.S., and Rinn, J.L.** (2014). The dynamics and regulators of cell fate decisions are revealed by pseudotemporal ordering of single cells. *Nat. Biotechnol.* **32**: 381–386.
- Van Damme, D., De Rybel, B., Gudesblat, G., Demidov, D., Grunewald, W., De Smet, I., Houben, A., Beeckman, T., and Russinova, E.** (2011). *Arabidopsis*  $\alpha$  Aurora kinases function in formative cell division plane orientation. *Plant Cell* **23**: 4013–4024.
- Vandepoele, K., Raes, J., De Veylder, L., Rouzé, P., Rombauts, S., and Inzé, D.** (2002). Genome-wide analysis of core cell cycle genes in *Arabidopsis*. *Plant Cell* **14**: 903–916.
- Winter, D., Vinegar, B., Nahal, H., Ammar, R., Wilson, G.V., and Provar, N.J.** (2007). An “Electronic Fluorescent Pictograph” browser for exploring and analyzing large-scale biological data sets. *PLoS One* **2**: e718.
- Wolf, F.A., Hamey, F., Plass, M., Solana, J., Dahlin, J.S., Gottgens, B., Rajewsky, N., Simon, L., and Theis, F.J.** (2018). Graph abstraction reconciles clustering with trajectory inference through a topology preserving map of single cells. *bioRxiv* .
- Wolock, S.L., Lopez, R., and Klein, A.M.** (2018). Scrublet: Computational identification of cell doublets in single-cell transcriptomic data. *bioRxiv* <https://www.biorxiv.org/content/10.1101/357368v1>.
- Yost, H.J., and Lindquist, S.** (1986). RNA splicing is interrupted by heat shock and is rescued by heat shock protein synthesis. *Cell* **45**: 185–193.
- Yost, H.J., and Lindquist, S.** (1988). Translation of unspliced transcripts after heat shock. *Science* **242**: 1544–1548.
- Zhu, D., Wu, Z., Cao, G., Li, J., Wei, J., Tsuge, T., Gu, H., Aoyama, T., and Qu, L.J.** (2014). TRANSLUCENT GREEN, an ERF family transcription factor, controls water balance in *Arabidopsis* by activating the expression of aquaporin genes. *Mol. Plant* **7**: 601–615.